Charge distribution near bulk oxygen vacancies in cerium oxides

TOPICAL REVIEW

Charge distribution near bulk oxygen vacancies in cerium oxides

E Shoko, M F Smith and Ross H McKenzie

Department of Physics, The University of Queensland, Brisbane, QLD 4072, Australia

E-mail: uqeshoko@uq.edu.au

Abstract
Understanding the electronic charge distribution around oxygen vacancies in transition metal and rare earth oxides is a scientific challenge of considerable technological importance. We show how significant information about the charge distribution around vacancies in cerium oxide can be gained from a study of high resolution crystal structures of higher order oxides which exhibit ordering of oxygen vacancies. Specifically, we consider the implications of a bond valence sum analysis of Ce_7O_{12} and $Ce_{11}O_{20}$. To illuminate our analysis we show alternative representations of the crystal structures in terms of orderly arrays of coordination defects and in terms of fluorite-type modules. We found that in Ce_7O_{12}, the excess charge resulting from removal of an oxygen atom delocalizes among all three triclinic Ce sites closest to the O vacancy. In $Ce_{11}O_{20}$, the charge localizes on the next nearest neighbour Ce atoms. Our main result is that the charge prefers to distribute itself so that it is farthest away from the O vacancies. This contradicts *the standard picture of charge localization* which assumes that each of the two excess electrons localizes on one of the cerium ions nearest to the vacancy. This standard picture is assumed in most calculations based on density functional theory (DFT). Based on the known crystal structure of Pr_6O_{11}, we also predict that the charge in Ce_6O_{11} will be found in the second coordination shell of the O vacancy. We also extend the analysis to the Magnéli phases of titanium and vanadium oxides (M_nO_{2n-1}, where M = Ti, V) and consider the problem of metal–insulator transitions (MIT) in these oxides. We found that the bond valence analysis may provide a useful predictive tool in structures where the MIT is accompanied by significant changes in the metal–oxygen bond lengths. Although this review focuses mainly on bulk cerium oxides with some extension to the Magnéli phases of titanium and vanadium, our approach to characterizing electronic properties of oxygen vacancies and the physical insights gained should also be relevant to surface defects and to other rare earth and transition metal oxides.

(Some figures in this article are in colour only in the electronic version)

Contents

1. Introduction

Non-stoichiometric phases of a number of transition metal and rare earth oxides have become widely studied in the past decade because of their potential in technological applications. Important examples are derived from the 'parent' materials TiO_2, VO_2, ZrO_2, HfO_2, CeO_2, by doping with metal ions or reduction by removal of oxygen atoms. A key scientific question in all these materials is the structure and electronic properties of oxygen vacancies. Ceria (cerium oxide) is a technologically important material with applications in high temperature electrochemical devices [1–5], catalysis [6–9], oxygen gas sensors [10, 11], and magnetic semiconductors [12, 13]. A fundamental property of this material relevant to all of these applications is its oxygen storage capacity (OSC). The material can rapidly take up and release oxygen through a reversible chemical reaction. There has been a considerable multi-disciplinary research effort aimed at developing a fundamental picture of the microscopic processes associated with this reversible chemical reaction. Key questions include:

(i) What is the *origin* of the reversible uptake and release of oxygen by ceria?
(ii) What is the *origin* and *mechanism* of the anionic conduction?
(iii) What is the *nature*, *composition* and *geometry* of the catalytically active sites on cerium oxide surfaces?
(iv) What is the *nature* of oxygen vacancies in the bulk solid and on surfaces?
(v) When an oxygen atom is removed to create a vacancy, *what happens to the two electrons that are left behind*?

Similar questions are also important in other oxides. The larger part of this review is primarily concerned with the last two questions and the study is restricted to the case of bulk ceria. In this introduction, we briefly outline the current understanding of the problem with respect to the last two questions. We also include in this review, a discussion of the Magnéli phases of titanium and vanadium in order to illustrate how our approach is also relevant to other areas of physics, namely, metal–insulator transitions. Throughout this review, we assume that the solids are in equilibrium and overall electroneutral. We mention this because of some recent discussion, albeit in different material systems, of deviations from electroneutrality [14, 15].
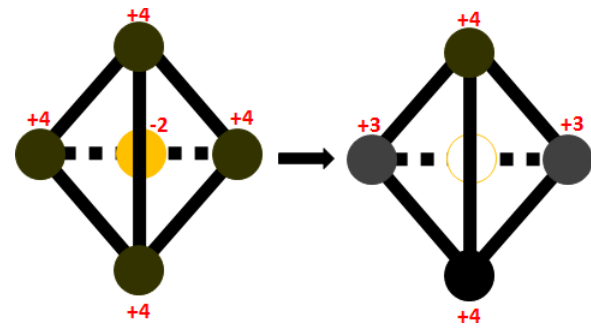
Figure 1. Schematic of the standard picture of charge redistribution following the formation of an oxygen vacancy in CeO_2. The tetrahedron of Ce atoms (black circles) with an O atom at its centre (grey (orange in colour version) circle) is shown along with the charges on these atoms in the simple ionic picture description of CeO_2. The process of reduction shown by the arrow leads to a neutral O vacancy at the centre of the tetrahedron (empty circle) while two of the Ce ions have been reduced to the 3+ oxidation state.

When CeO_2 is reduced to the various defective phases, CeO_{2-x}, according to equation (1), O vacancies are formed in the lattice structure.

$$CeO_2 \rightleftharpoons CeO_{2-x} + \frac{x}{2}O_2(g), \qquad 0 \leqslant x \leqslant 0.5. \quad (1)$$
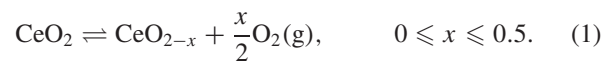
The crystal structure adopted by any such defective phase, CeO_{2-x}, is understood to be the one that provides the most favourable energetics for the arrangement of all the O vacancies within the structure. In a widely accepted view of the microscopic description of O vacancy formation and ordering in CeO_{2-x} phases, the two electrons associated with a missing O atom when an O vacancy forms fully localize on two of the four equivalent Ce^{4+} ions which form a tetrahedron around the vacancy site, as shown in equation (2) [16, 17, 6, 18]:

$$4Ce_{Ce} + O_O \rightleftharpoons 2Ce_{Ce} + 2Ce'_{Ce} + V_{\ddot{O}} + \tfrac{1}{2}O_2(g) \quad (2)$$

where we have used the Kroger–Vink notation [19] so that the symbols have the following meanings: Ce_{Ce}—a Ce^{4+} ion on a Ce lattice site, O_O–O^{2-} ion on an O lattice site, Ce'_{Ce}—a Ce^{3+} ion on a Ce lattice site and $V_{\ddot{O}}$—neutral O vacancy site. This mechanism, which we will henceforth refer to as the standard picture, is illustrated in the schematic in figure 1. The localization of an electron on a Ce^{4+} ion converts it to the slightly larger Ce^{3+} ion with one electron in the 4f orbital. In the reverse process where a defective phase, CeO_{2-x}, is oxidized, two 4f electrons from the two neighbouring Ce^{3+} ion sites move onto the site where an O atom is incorporated and then delocalize into the O 2p valence band. Thus, the reversible processes of oxidation and reduction in equation (1) have been considered to involve the extremal states of the Ce 4f electrons in which they are fully delocalized and fully localized respectively [17].

There have been, broadly speaking, three different approaches for investigating this problem. Crystallographers have attempted to establish general principles for O vacancy ordering in the reduced ceria phases. In 1974, Martin proposed the coordination defect model [20]. He suggested that when

an O vacancy is created in the lattice of a rare earth oxide, the local environment of the vacancy undergoes relaxations in such a way that the four nearest neighbour Ce and six nearest neighbour O atoms form a stable structural entity which is referred to as a coordination defect. The crystal structures of the higher rare earth oxides are then determined and restricted by the topology of this coordination defect. In 1996, Kang and Eyring developed a different framework for describing vacancy ordering based on structural elements which are derived from the conventional unit cell of CeO_2 in a simple way [21]. As will be described in more detail later, there are thirteen of these structural elements, called modules, and they are the fundamental building blocks for all the crystal structures of the higher oxides in the Kang–Eyring fluorite-type module theory. As a result, it is possible to define what has been called a modular unit cell in which, instead of the usual atomic basis, the different modules form the basis. The value of this approach is the simplicity and elegance with which it provides insight into the superstructures observed in the reduced higher oxides in relation to the parent fluorite structure from which they are derived.

Neither crystallographic approach sought to explicitly account for the charge redistribution that occurs when an O vacancy is formed. However, as we will show, they provide useful vantage points from which to examine the problem. In contrast, the remaining two approaches in the strategy sought to specifically establish the nature and occupation of the Ce 4f level in the Ce oxides and consequently, the charge redistribution that occurs when an oxygen vacancy is created. The earliest literature in this direction emerged from spectroscopists [22], with their results being interpreted using either cluster models [23] or the single impurity Anderson model [24–26]. This work investigated the occupation of the Ce 4f level in the two extremal phases, CeO_2 and Ce_2O_3 and it was concluded that CeO_2 is mixed valence whereas Ce_2O_3 is a pure $4f^1$ configuration. The result that CeO_2 is mixed valence is inconsistent with the ionic description underlying the standard picture. However, the models used to interpret the spectroscopic results are not parameter-free and the conclusions drawn from them have been contested [27].

Recently electronic structure calculations based of density functional theory (DFT) have been performed. In general, DFT results for CeO_2 assume empty Ce 4f states, which is the simple ionic picture of bonding in this oxide, e.g., [28]. To describe vacancy formation in CeO_2, the simplest case to consider is a $2 \times 2 \times 2$ supercell of CeO_2 from which a single O atom is removed. This supercell has the composition $Ce_{32}O_{63}$ ($CeO_{1.97}$). As this composition does not correspond to any known phases of reduced ceria, it is customary to require the structural parameters of the relaxed structure to match those of CeO_2 based on Vegard's rule [29], i.e., there is a linear relationship between the lattice constant and the extent of reduction. As will be discussed in more detail in section 4.3, most of the DFT work supported the standard picture. However, the approximate functionals of DFT such as LDA, GGA, and LDA $+$ U do not appear to describe well the electronic properties of the reduced phases [30–32]. Furthermore, recent calculations using hybrid functionals [33]

and DFT $+$ U [32–34] do not appear to support the standard picture.

As far as we know, a study of the charge distribution near bulk O vacancies in crystallographic phases of reduced cerium oxide apart from Ce_2O_3 (and the customary supercell of DFT calculations, i.e., $CeO_{1.97}$) has not been done. Our study of the charge distribution in the well-characterized intermediate phases represents a complementary approach to answering the fundamental question of where the two electrons left behind when an O vacancy forms go. Furthermore, since no *in situ* studies have been done to identify the precise phases involved in ceria-based catalysis, it is also possible that the intermediate phases may play an important role in the engineering applications of these materials.

In this study, we examine the standard picture for the oxidation and reduction in ceria described above, considering primarily two intermediate phases namely $Ce_{11}O_{20}$ and Ce_7O_{12}. A brief discussion of Ce_6O_{11} is also included. We discuss this in light of our recent results on Ce site valencies obtained by an analysis of observed crystal structures using the bond valence method [35]. The two cases, $Ce_{11}O_{20}$ and Ce_7O_{12}, were chosen to illustrate the evolution of the charge distribution around O vacancies that occurs with reduction. Furthermore, apart from the extremal structures, namely CeO_2 and Ce_2O_3, these two examples along with Ce_3O_5 were the only crystal structures of the Ce oxides for which we were able to obtain highly accurate crystallographic data to enable the type of analysis we do here.

As is discussed later, both $Ce_{11}O_{20}$ and Ce_7O_{12} have fluorite-related crystal structures. According to Kang and Eyring, Ce_7O_{12} is the limiting intermediate oxide for which any further reduction leads to loss of the fluorite structure of CeO_2 [36]. However, the fluorite-related Ce_3O_5 phase was recently observed in the phase diagram of the Ce–O system [37]. In addition to the conventional unit cells, we will generally use the Kang and Eyring structural principle of modular units to discuss O vacancy ordering in reduced ceria phases [36, 21, 38, 39]. There will be occasional references to Martin's coordination defect model [20, 16, 40] where this model may provide a better conceptual framework.

This paper is organized as follows: in section 2 we present the crystal structures of $Ce_{11}O_{20}$ and Ce_7O_{12} both in the conventional way as well as in the representation of the Kang–Eyring fluorite-type module theory. We show how the Kang–Eyring fluorite-type module theory helps to understand the structure of O vacancies in $Ce_{11}O_{20}$ and Ce_7O_{12} in relation to the parent fluorite structure. In section 3, we consider the implications of our bond valence calculations for the charge distribution in the local environment of the O vacancies. Section 4 discusses how our results conflict with the standard picture of charge localization in reduced ceria phases. We then make a prediction of the charge distribution to be expected in the Ce_6O_{11} crystal based on the bond valence model in section 5. The possibility of direct f–f coupling between neighbouring Ce sites in crystals of the Ce oxides. We assess the validity of this idea from the Harrison method of universal parameters in section 6. Section 7 examines the usefulness of bond valence analyses in understanding metal–insulator
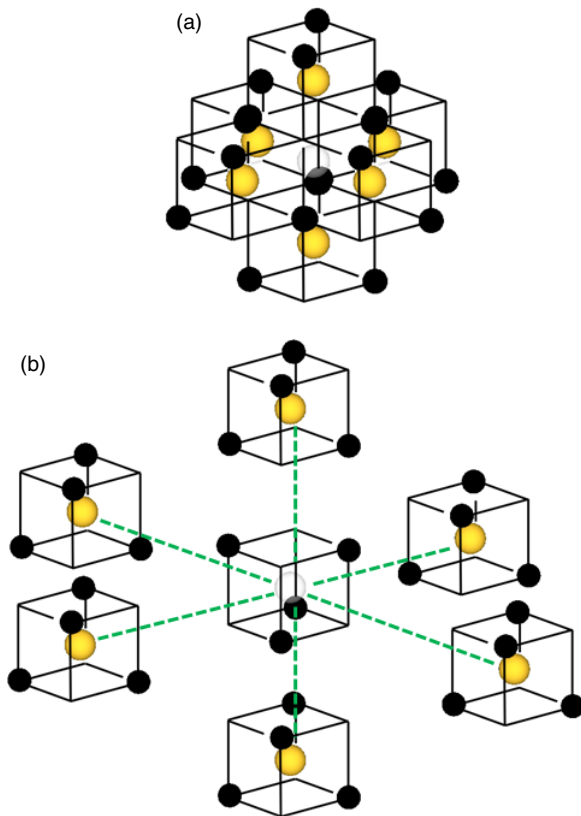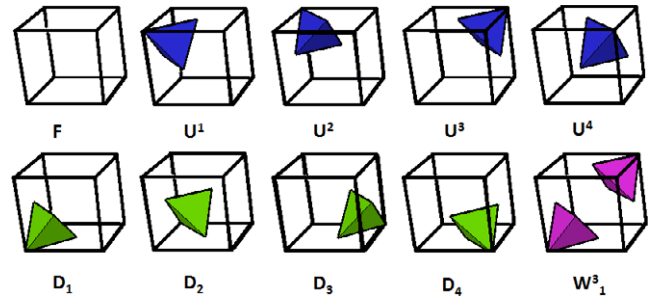
Figure 2. (a) Coordination defect showing characteristic topology. (b) Exploded view of the coordination defect showing the central octant of what is called the 'λ phase' coordinated by six $M_{\frac{1}{2}}O$ octants of what is called the 'δ phase'. The λ phase only differs from the δ phase in that it has an O vacancy as shown. Black circles represent Ce atoms, grey (orange in colour version) circles—O atoms and the light grey circle inside the λ phase is an O vacancy. Adapted from Martin [41].

Figure 3. The ten different modules required to build the modular unit cells of $Ce_{11}O_{20}$ and Ce_7O_{12}. The vertices of the tetrahedra denote the locations of the Ce ions surrounding an O vacancy. Module F is the conventional unit cell of CeO_2. Except for W_1^3 which has two O vacancies along the body diagonal of the CeO_2 unit cell, the rest of the modules have only one O vacancy in the positions shown. Adapted from Kang and Eyring [36].
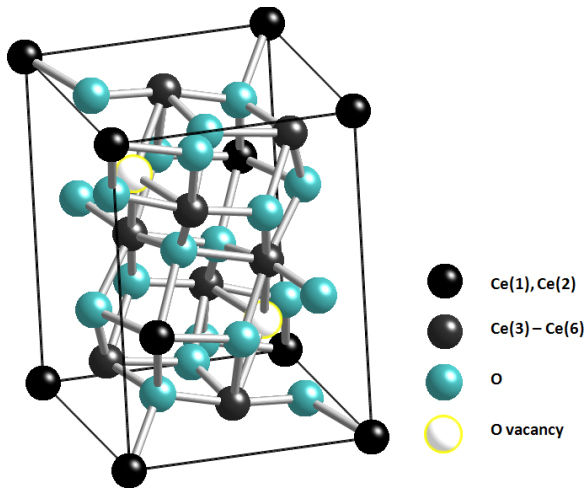
coordination defect. This model, in its original formulation, does not explicitly account for the changes in the valences of the Ce ions and the four Ce ions which are nearest neighbours to the O vacancy in the coordination defect are implicitly identical.

2.2. Modules

Soon after the elaboration of Martin's coordination defect model [16], Kang and Eyring developed a simpler model for constructing the crystal structures of the higher rare earth oxides, i.e., oxides from Ce_7O_{12} to CeO_2 based on a different set of structural elements [21]. These so-called modules, include the CeO_2 unit cell, with the rest derived from it by creating one or two O vacancies in certain prescribed ways, resulting in a total of thirteen modules. These modules are the fundamental building blocks for all the higher oxides under a prescription of rules defined by the authors [36]. In figure 3, we show the ten modules relevant to $Ce_{11}O_{20}$ and Ce_7O_{12} in addition to the unit cell of CeO_2. Kang and Eyring's method accounted for all the higher oxides known at the time and was successful in predicting the existence of new structures [36]. The Kang and Eyring method enables a relatively simple way of visualizing vacancy sites which are otherwise difficult to decipher when the structure is cast in the conventional setting of its space group. This provides considerable facility in the analysis of the local environment of the O vacancy site. As a result, we will make frequent reference to this framework in the rest of this paper.

2.3. $Ce_{11}O_{20}$

The conventional unit cell of $Ce_{11}O_{20}$ is shown in figure 4. Note that for all ball and stick figures in this paper, the sticks between the Ce sites and the O vacancy site do not represent chemical bonds. Instead, the sticks are only included to show the geometric relationships between the atoms. The unit cell of $Ce_{11}O_{20}$ consists of one formula unit per unit cell with inversion as its point group symmetry. It has six Ce and ten O distinct sites along with their inversion images with the Ce(1) site as the centre of inversion. However, for a

transitions using titanium and vanadium Magnéli phases as examples. Conclusions are presented in section 8.

2. Alternative representations of the crystal structures of $Ce_{11}O_{20}$ and Ce_7O_{12}

2.1. Coordination defect model

Martin proposed describing an O vacancy in a Ce oxide crystal as a structural entity made up of 4 Ce ions and 6 O ions around the vacancy site, as illustrated in figure 2 [20, 16]. The four Ce ions form the first coordination shell (a tetrahedron) of the vacancy site while the six O atoms form the second coordination shell (an octahedron). Compared to the perfect structure of CeO_2, all four Ce ions are displaced 0.2 Å away from the vacant O site, while the O atoms are shifted 0.3 Å towards the vacancy. This structural unit has been called the coordination defect and it maintains its structural integrity in a crystal of the oxide (see figure 2). It is constructed from two types of subunits called octants, one of composition $Ce_{\frac{1}{2}}O$ called the δ phase and the other incorporating an O vacancy, the λ phase, of composition $Ce_{\frac{1}{2}}$. The exploded view in figure 2 (b) shows these octants and how they are arranged to form the

Figure 4. The unit cell of $Ce_{11}O_{20}$ whose space group is $P\bar{1}$. There are six distinct Ce sites in this crystal. However, to facilitate the discussion of vacancy structures and charge distribution, the Ce sublattice has been partitioned into two types of lattice points, as shown in the legend. The first set of lattice points consists of the Ce(1) and Ce(2) sites which, if we only consider the Ce sublattice, occupy the second coordination shells of the O vacancies. The second set consists of the remainder of the Ce sites and these form the first coordination shell of the O vacancies in the Ce sublattice of the crystal. There are ten distinct O sites in the crystal, but for our purposes, it is convenient to treat all the O sites in the O sublattice as roughly equivalent, as indicated in the legend.

description of the vacancy structure and charge distribution in this crystal, it is convenient to view all the lattice points in the O sublattice as roughly equivalent and to divide the Ce sublattice into two regions. The first region consists of the Ce(1) and Ce(2) sites which, in the Ce sublattice, occupy the second coordination shells of the O vacancies. The remainder of the Ce atoms are the first coordination shells of the O vacancies. The crystal structure of $Ce_{11}O_{20}$ can be readily related to the fluorite structure of CeO_2 from which it is derived by reduction. This relationship becomes clearer with the Kang–Eyring module representation. Kang and Eyring [36] have shown that the modular unit cell of $Ce_{11}O_{20}$ has the modular composition 3F, 4D, 4U where the module types are as given in figure 3. They also provided the modular sequences for the [100] and [010] directions in this crystal as $FFU^3U^2D_3D_2FU^4U^1D_4D_1$ and $FU^3D_3FU^1D_1FU^2D_2U^4D_4$ respectively. Using this information along with their module juxtaposition rules, we derived the modular sequence for the [001] direction to be $D_1D_2FFFU^4U^3U^1U^2D_4D_3$. This then enabled us to construct the 3D modular unit cell of $Ce_{11}O_{20}$ shown in figure 5. We note that this unit cell is not unique. There is only one type of O vacancy in the crystal of $Ce_{11}O_{20}$ and if we only consider the Ce sublattice, each O vacancy has the four Ce(3)–Ce(6) sites forming its first coordination shell. These four Ce sites form a distorted tetrahedron. The O vac–Ce(i) distances are shown in table 1 where i = 3–6. The second coordination shell consists of twelve Ce sites namely, two Ce(1), four Ce(2), two Ce(3), two Ce(4) and one of each of the Ce(5) and Ce(6) sites as shown in table 1. Of these twelve Ce sites in the O vacancy's second coordination shell,
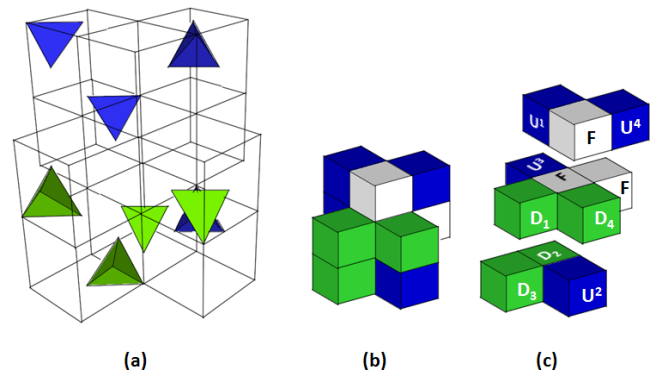

Figure 5. The fluorite-type modular unit cell of $Ce_{11}O_{20}$ derived using the Kang and Eyring rules [36]. In (a), the modular unit cell is constructed from transparent modules to show the location of the O vacancy site, as indicated by the shaded tetrahedra with the module types as identified in (c) and shown in detail in figure 3. A simplified block representation of the modular unit cell given in (a) is shown in (b). The exploded view with all the module types identified is given in (c). The modular composition is: top layer—U^1, F, U^4; middle layer—D_1, D_4, F, F, U^3; bottom layer—D_2, D_3, U^2. These figures make clear the distribution of the O vacancies within the crystal in relation to the original fluorite structure. There are large contiguous regions, modules F, where there are no O vacancies.

Table 1. The first- and second coordination shells of the O vacancy in the Ce sublattice of $Ce_{11}O_{20}$ and some selected distances between the sites. These Ce–Ce distances show that the average intra-tetrahedral separation between Ce sites (4.2 Å) is larger than the inter-tetrahedral separation (3.9 Å).

Ce site	Distance from O vacancy (Å)	Direct Ce–Ce type	Direct Ce–Ce distance (Å)
First coordination			
Ce(6)	2.5106	Ce(6)–Ce(3)	4.169
Ce(3)	2.5674	Ce(6)–Ce(4)	4.194
Ce(4)	2.5817	Ce(6)–Ce(5)	4.207
Ce(5)	2.6185	Ce(3)–Ce(4)	4.219
		Ce(3)–Ce(5)	4.144
		Ce(4)–Ce(5)	4.234
Second coordination			
Ce(5)	4.3184	Ce(1)–Ce(5)	3.810
Ce(4)	4.4140	Ce(1)–Ce(4)	6.904
Ce(3)	4.4164	Ce(1)–Ce(3)	3.852
Ce(3)	4.4341		
Ce(4)	4.4390		
Ce(6)	4.4438	Ce(1)–Ce(6)	5.561
Ce(2)	4.4952	Ce(1)–Ce(2)	7.715
Ce(2)	4.5265	Ce(2)–Ce(3)	3.873
Ce(2)	4.5340	Ce(2)–Ce(4)	3.861
Ce(1)	4.5579	Ce(2)–Ce(5)	6.860
Ce(1)	4.5705	Ce(2)–Ce(6)	5.573
Ce(2)	4.6007		

only half a Ce(1) site and one Ce(2) site can be assigned to the particular O vacancy site. Thus, in total, an O vacancy in $Ce_{11}O_{20}$ is proportionately associated with five and half Ce sites. It is convenient to work with an integral number of Ce sites when studying the charge distribution in the local environment of an O vacancy. In order to do this, we propose to partition the lattice so that we consider a vacancy cluster consisting of two neighbouring O vacancies which can then
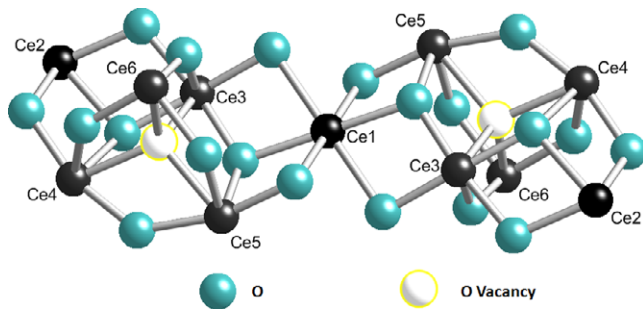
Figure 6. The proposed vacancy cluster of $Ce_{11}O_{20}$ consisting of two O vacancies which are nearest neighbours and related to each other by inversion symmetry centred on the Ce(1) site.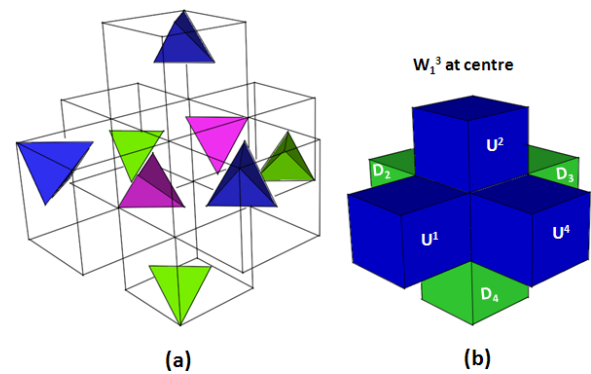 The various Ce sites are labelled as shown. The white and light grey (teal) circles represent O vacancies and various O sites, respectively.

Figure 7. The unit cell of Ce_7O_{12} showing the two distinct Ce sites: Ce(1)—black and Ce(2)—dark grey. The O(1) sites are shown in grey (teal) with the O(2) light grey (orange). The Ce(1) and Ce(2) sites are of S_6 and i symmetries, respectively. The O vacancy sites are shown in white. A characteristic structural unit of the Ce_7O_{12} crystal is the divacancy, which consists of two O vacancy sites connected by an S_6 Ce site between them.

be associated with eleven Ce sites. Since the choice of the Ce(1) site is the most difficult to establish, we pick a Ce(1) site and construct the vacancy cluster around it. A Ce(1) site has four closest O vacancies all in the third coordination shell. Two of the O vacancies are located 4.558 Å away from the Ce(1) lattice point with the other two at 4.571 Å. Since the Ce(1) site is a centre of inversion, each of these pairs of O vacancies are related by inversion symmetry. We choose the pair with the shortest distance from the Ce(1) site to define the vacancy cluster consisting of two O vacancies. The cluster obtained by this procedure is illustrated in figure 6. This cluster should not be confused with the divacancy of Ce_7O_{12} to be discussed later. The divacancy of Ce_7O_{12} is a unique structural entity of the crystal arising from long range ordering of the vacancies whereas the cluster we define here is simply an analytic convenience. It cannot be strictly considered to be specified in a unique way since the pair of O vacancies we chose is only 0.01 Å closer to the Ce(1) compared to the other. On the O vacancy sublattice, each O vacancy has four nearest neighbours 6.134 Å away for the first pair and 6.138 Å for the second. There is no difficulty in identifying the Ce(2) site associated with each O vacancy since there is only one closest (4.495 Å) Ce(2) site. The distances are calculated from the crystallographic data of Kummerle and Heger [42]. Zhang *et al* [43] suggested another useful way of viewing the crystal structure of $Tb_{11}O_{20}$ which is also directly applicable to $Ce_{11}O_{20}$ because these compounds are isostructural. Their perspective is based on the observation that the O vacancies are more or less uniformly distributed within the crystal structure with no evidence of vacancy pairing. The vacant O sites are distributed in a way such that the separation between the defects is maximized and thus, the repulsive interactions are reduced. The Ce ions in the first coordination shell relax outward in a more or less isotropic way (Ce–$V_{\ddot{O}}$ ranges 2.51–2.62 Å, see table 1). As the vacant Ce tetrahedra expand, the regions between them experience substantial compression, as indicated by the difference in the distances between the intra-tetrahedral ions (4.2 Å) and those of the inter-tetrahedral ions (3.9 Å). These distances are given in table 1. In this table, the intra-tetrahedral ion distances are given as the direct Ce–Ce distances in the first coordination shell while the inter-tetrahedral ion distances refer to these distances in the

Figure 8. (a) The modular unit cell of Ce_7O_{12} showing the details of the seven modules used to construct it. Each tetrahedron represents the four Ce atoms around the oxygen vacancy. (b) A simplified model of the modular unit cell. Adapted from Kang and Eyring [36].

second coordination shell: Ce(1)–Ce(5), Ce(1)–Ce(3); Ce(2)–Ce(3) and Ce(2)–Ce(4). The inter-tetrahedral Ce ions have a coordination number of eight as in the parent fluorite structure. In discussing the charge distribution in the local environment of the vacancy, we will notice that the charge is distributed in a manner which is distinctly different between the intra-tetrahedral and inter-tetrahedral Ce ions.

2.4. Ce_7O_{12}

Figure 7 shows the unit cell of Ce_7O_{12} in the conventional rhombohedral setting. In the Kang–Eyring framework, the modular composition of this crystal is D_2, D_3, D_4, W_1^3, U^1, U^2 and U^4 [36]. The modular unit cell constructed from this basis is depicted in figure 8. It is readily apparent from figure 8 where the O vacancy sites are located. There are two types
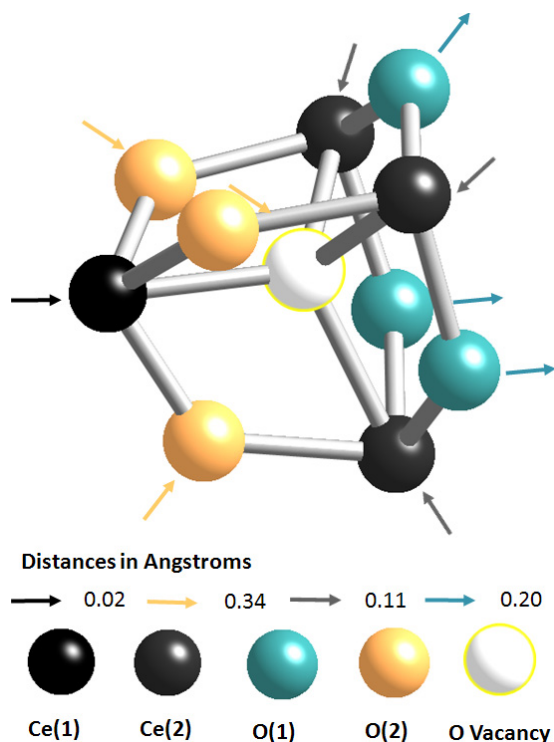
Figure 9. The relaxation of atoms forming part of the divacancy in Ce_7O_{12}. The different lattice sites are indicated by the colours as follows: Ce(1)—black, Ce(2)—dark grey, O(1)—grey (teal), O(2)—light grey (orange) and the O vacancy ($V_{\ddot{O}}$)—white. The arrows indicate the direction in which the respective atoms relax relative to the O vacancy site and the amounts by which the 'bonds' relax are shown in the legend. This figure was produced from the crystal structure determined by neutron scattering [42].

of Ce sites, Ce(1) and Ce(2), in the crystal lattice of Ce_7O_{12}, which are of S_6 and i symmetry respectively [44, 42]. These distinct sites are indicated in the conventional unit cell of figure 7. Although Kang and Eyring did not explicitly identify the distinct sites in their modular unit cell according to their symmetries, it is apparent that by translating their unit cell in three dimensions, two distinct Ce sites are obtained; the S_6 site with two nearest neighbour O vacancies around it and the i site with only one O vacancy. The S_6 site has been called the divacancy site [36] and it forms a shared corner between two coordination tetrahedra of the O vacancies, as illustrated in figure 11. We list here some interatomic distances that we will use in our analysis of the divacancy cluster: Ce(2)–Ce(2) = 4.09 Å, Ce(1)–Ce(2) = 4.11 Å, Ce(1)–O(2) = 2.19 Å and for Ce(2)–O(1), there are two relevant bond lengths, namely 2.23 and 2.32 Å. The Ce–Ce distances are direct distances between these sites, not distances along the Ce–O bonds connecting them. It appears that the Ce sublattice has not changed much relative to CeO_2.

It is helpful to visualize vacancy ordering in Ce_7O_{12} by viewing the divacancy as a structural unit of the O vacancies in this crystal. This clarifies why the ratio of S_6 to i sites is 1:6; all the Ce sites which are nearest neighbours to the two O vacancies forming a divacancy are of S_6 symmetry. As there are seven Ce atoms in the formula unit, the rest of the Ce atoms (six) must be the Ce(2) sites of i symmetry. The
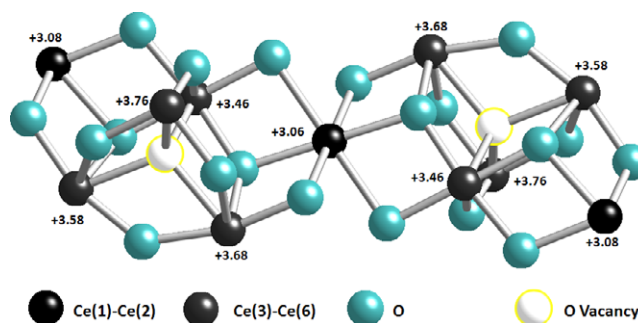
Figure 10. Charges of the different Ce ions in the vacancy cluster of $Ce_{11}O_{20}$ obtained from the bond valence model. The vacancy cluster consists of two vacancies connected by the Ce(1) site which is also a centre of inversion for the cluster. The four excess electrons that arise due to the removal of the two oxygen atoms do not localize on the cerium atoms nearest the vacancies. This is contrary to the standard picture.

formation of the divacancy structures as CeO_2 is reduced to Ce_7O_{12} is associated with some relaxation of the crystal lattice, although the Ce sublattice remains somewhat invariant [36]. We now examine this relaxation process, which is illustrated in figure 9 and based on Kummerle and Heger's neutron diffraction data [42]. The bond lengths in CeO_2 are 2.434 Å and 2.706 Å for the Ce–O and O–O bonds respectively. When a divacancy is formed, the bonds within the divacancy relax and diffraction data show that in Ce_7O_{12} the 'bond' lengths are [42]: 2.505 Å for O(1)–$V_{\ddot{O}}$, 2.364 Å for O(2)–$V_{\ddot{O}}$, 2.418 Å for Ce(1)–$V_{\ddot{O}}$ and 2.543 Å for Ce(2)–$V_{\ddot{O}}$. This structural data indicates that compared to CeO_2, the bonds within the divacancy have changed as follows: the O(1)–$V_{\ddot{O}}$ and O(2)–$V_{\ddot{O}}$ 'bonds' contract by 0.20 Å and 0.34 Å respectively while the Ce(2)–$V_{\ddot{O}}$ 'bond' gets longer by 0.109 Å. The Ce(1)–$V_{\ddot{O}}$ 'bond' is practically unchanged, showing only a small contraction of about 0.02 Å. Thus, we see that, just as was the case for $Ce_{11}O_{20}$, the O atoms are attracted to the vacancy site while the Ce(2) atoms are repelled away so that the O atoms now become the nearest neighbours of the vacancy site. This appears to be a general feature of vacancies in rare earth higher oxides [16, 36]. We note that the six O atoms around the vacancy relax by different amounts with the O(2) atoms being more strongly attracted to the vacancy site. We also note that according to the coordination defect model, the crystal structure of Ce_7O_{12} has the highest packing density of the coordination defect.

3. Excess electrons delocalize away from the oxygen vacancy

Having discussed the O vacancy ordering in $Ce_{11}O_{20}$ and Ce_7O_{12} as well as proposing some vacancy clusters suitable for the analysis of charge distribution in these crystals in the section 2, we now present the results of the bond valence calculations, **I**, in these clusters.

3.1. $Ce_{11}O_{20}$

Figure 10 shows the bond valence sums on the various Ce sites in the vacancy cluster of $Ce_{11}O_{20}$ which was introduced
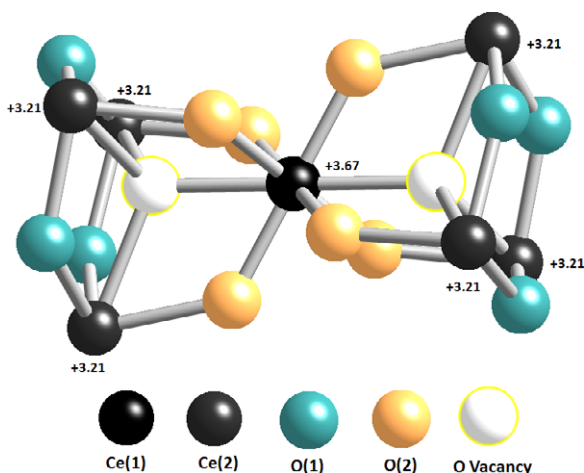
Figure 11. The divacancy of Ce_7O_{12} showing the valences of the Ce atoms calculated from the bond valence model, **I**. The charge delocalizes on the three Ce(2) sites of triclinic symmetry which now have a valence of $+3.21$.

earlier, see figure 6. Clearly the charge from the vacancy does not localize on the Ce sites closest to the vacancy but rather, delocalizes onto the Ce(1) and Ce(2) sites. This contradicts the standard picture. The results of figure 10 can be compared with those of $Tb_{11}O_{20}$ with which it is isostructural. Based on a simple consideration of the crystal radii of the cations [45], Zhang *et al* [43] suggested the following valencies for the cations: Tb(1) and Tb(2)—+3, Tb(3) and Tb(4)—+3.75, Tb(5) and Tb(6)—+4. Here the numbering of the sites is the same as for $Ce_{11}O_{20}$ given in figure 6. Their assignment of the site valences qualitatively agrees well with our bond valence results for $Ce_{11}O_{20}$. The Tb^{3+} and Tb^{4+} ions are f^8 and f^7 configurations respectively and can be compared to the corresponding f^1 and f^0 configurations respectively for the Ce ions. They suggested the possibility of fast electron transfer between the neighbouring Tb(2) sites so that, instead of two $Tb(2)^{3+}$ and one $Tb(2)^{4+}$ instantaneous states, an average is obtained from the neutron diffraction data. It was suggested by the authors that the thermal ellipsoids of the atoms in Ce_7O_{12}, which are much higher than in CeO_2, could be evidence of the dynamic disorder arising from the fast electron transfer.

3.2. Ce_7O_{12}

The charge distribution in the divacancy of Ce_7O_{12} is shown in figure 11. This figure clearly shows that, apart from the Ce(1) site which is of a different local site symmetry compared to the Ce(2) sites, the charge delocalizes over all three of the Ce atoms closest to the vacancy. Again, this contradicts the standard picture, which has the electrons completely localized on two of the neighbouring Ce atoms.

In **I**, we pointed out that a naive consideration of the stoichiometric valence of a compound may not be adequate to describe the charge distribution in Ce oxides. The above discussion on Ce_7O_{12} and $Ce_{11}O_{20}$ demonstrates this point clearly. The simple stoichiometric valence approach strictly assigns integral valences to ions in a compound and, thus, assumes that the charge is fully localized on these sites. On

the other hand, when one calculates an *average* stoichiometric valence, the assumption that the charge fully delocalizes over the relevant ions is made. However, for a given compound, the reality may be quite different from either of these scenarios of perfect localization/delocalization of the charge [46]. As illustrated by the examples of Ce_7O_{12} and $Ce_{11}O_{20}$, it is possible within the same compound, to have sites where the charge is fully localized, others where it only partially localizes and yet others where it fully delocalizes. Recently Liebau *et al* proposed to distinguish between the stoichiometric valence of a compound and its structural valence, the latter being the valence obtained from the bond valence model [47]. The introduction of *structural valence* into the terminology is significant as this gives us a language for a concept which is more realistic in discussions of charge distribution in crystal structures.

4. Failure of the standard picture of charge localization near a vacancy

We now discuss the above results comparing them to the standard picture and propose an alternative view of how the charge redistributes itself following O vacancy formation in ceria as deduced from the bond valence model. As already mentioned, the conventional description of the electronic processes involved during O vacancy formation requires that the excess charge at the vacant O site be shared between two of the four Ce ions which form the first coordination shell of the vacancy. This means that the tetrahedron formed by the four Ce ions around the O vacancy consists of two Ce^{3+} and two Ce^{4+} ions. This description is based on the ionic model for these oxides, although Kang and Eyring do indicate that there may be some covalent character in these oxides [36].

4.1. $Ce_{11}O_{20}$

If we assume that the four electrons which are left when the two O vacancies are formed are localized within the cluster, then we can describe how the charge redistributes itself. In fact, from the bond valence results, which also showed mixed valence in CeO_2, the valence of Ce in CeO_2 is $+3.73$ and the corresponding valence of O is -1.87. A description of vacancy formation in CeO_2 to form $Ce_{11}O_{20}$ can then be illustrated in the bond valence model as shown in figure 12. Thus, according to the mixed valence description of the CeO_2 crystal from the bond valence model (see figure 12(a)), when an O vacancy is created in CeO_2, a charge of -1.87 is left behind as opposed to a charge of -2.0 in the ionic picture. This then means that, if we consider the vacancy cluster of figure 10 and equivalently, figure 12(b), the creation of the two O vacancies leaves a total charge of -3.74 in the cluster. From figure 10, we can see that compared to their original valences in CeO_2, the valences of Ce(5) and Ce(6) are virtually unchanged. Thus, considering the change in the valences of the remainder of the Ce sites, the total charge accumulation on the Ce sites in the cluster is -2.87. There is therefore a discrepancy of ~-1 between the total extra charge in the $Ce_{11}O_{20}$ crystal inferred from the bonding in CeO_2 (i.e. -3.74) and that directly calculated for this crystal
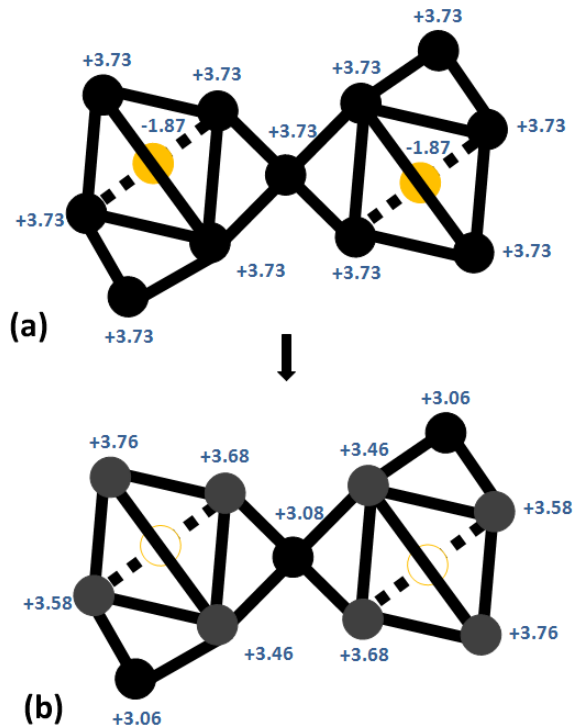
Figure 12. A schematic to illustrate the formation of $Ce_{11}O_{20}$ from CeO_2 through vacancy formation in the O sublattice. In (a), a part of the CeO_2 lattice, which, after removing the two O atoms (light grey (orange) circles), gives a cluster corresponding to the one given in figure 6. Also note that compared to figure 6, here we have made the further simplification of replacing all the Ce–O–Ce bonds with direct Ce–Ce bonds except for the two O atoms which are subsequently removed to create vacancies. For these two atoms, no bonding detail is given in the schematic, except that we place each of them at the centre of a regular Ce tetrahedron, reflecting their coordination environment in CeO_2. The numbers shown at the atomic sites are the valences of the respective atoms as determined by the bond valence method [35], and figure 10. In (b), the cluster of (a) after reduction to create the two O vacancies (empty circles). The colours in this figure denote the following: black circles—Ce sites which are not nearest neighbours to any O vacancies, grey circles—Ce atoms which are the nearest neighbours of at least one O vacancy, light grey (orange) circles—O atoms and empty circles—O vacancies.

by the bond valence calculations (-2.87). This discrepancy is entirely consistent with the accuracy of the bond valence model reported in **I**, although we note that the accounting of charge we have done here from CeO_2 to $Ce_{11}O_{20}$ is very simplistic. It ignores the many-body effects which may follow the injection of extra charge at the Ce sites when the O vacancies are created. Such an extra charge may change the degree of mixing between the Ce 4f- and the O 2p states in manner that may not be related in a simple way to their state in CeO_2. It may happen that, for instance, due to a change in the hybridization of Ce 4f- and the O 2p states, the extra charge may not be confined to the Ce 4f as we assumed in calculating the discrepancy in the total charge, but rather, some of the charge may go into the O valence band. It is expected that the results in figure 10 would capture these many-body effects. An important point from the results of figure 10 is that -1.99 ($\sim 70\%$) of the total charge of -2.87 goes to the three Ce atoms in the second coordination shell with the remainder being shared among the eight Ce atoms in the first coordination shell.

If one just considers the cation sublattice, it is evident that the charge accumulates in regions of high strain (inter-tetrahedral Ce ions) where the Ce–Ce distances are slightly shorter compared to the intra-tetrahedral case. This led some authors to consider the possibility that there may be some direct f–f hopping in these dense regions [43]. As we will discuss in section 6 for the case of Ce_7O_{12}, direct f–f hopping appears unlikely in these oxides.
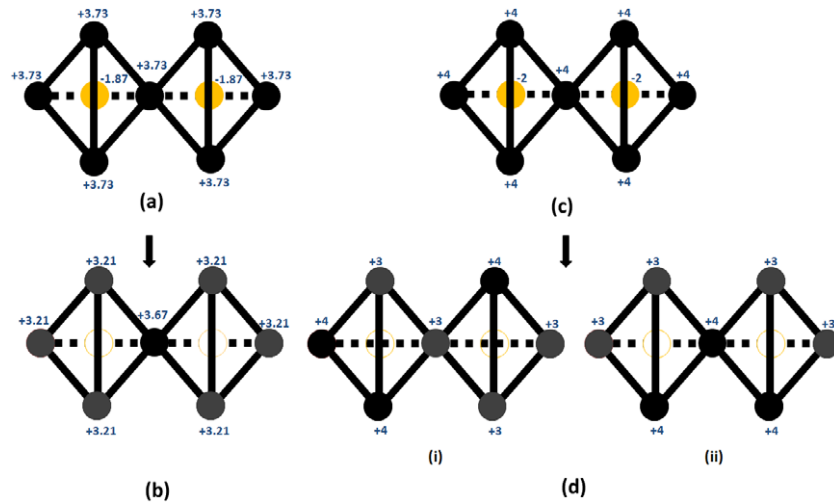
4.2. Ce_7O_{12}

Based on the results of figure 11, we can now discuss the electronic features of the local environment of the O vacancy in Ce_7O_{12}. The formation of the Ce_7O_{12} divacancy from the CeO_2 crystal lattice according to the BVM is schematically illustrated in figures 13(a) and (b). It can be seen that two corner-sharing Ce tetrahedra of CeO_2 lose an O atom each from the centre of the tetrahedron. Our bond valence calculations show that the valences of the Ce(1) and Ce(2) sites in Ce_7O_{12} are $+3.67$ and $+3.21$ respectively. The valence at the Ce(1) site is comparable to the value of $+3.73$ calculated for Ce in CeO_2 using a bond valence method analysis of the crystal structure. If we use the Kang and Eyring modular unit cell with its 8 O vacancies, 4 Ce(1) and 24 Ce(2) sites and further assume that we start from mixed valence CeO_2 where the valences are $+3.73$ and -1.87 for the Ce and O sites respectively, we can get some estimate of how the excess charge on the O vacancy sites is distributed in the modular unit cell. The valence of the Ce(1) sites does not change much from its value before the O vacancy is created. Thus, virtually all the charge left at the vacancy site by an O atom is evenly distributed within the first coordination shell of the vacancy site among the (three) Ce(2) sites. On this basis and only considering a simple analysis using the bond valence results for CeO_2, the valence at the Ce(2) sites is then readily calculated to be $+3.11$ (i.e., $3.73 - 1.87/3$) which is comparable to the independently calculated value of $+3.21$ within the error bounds (± 0.1) of the method. That the excess charge is not distributed evenly among all four of the Ce atoms in the first coordination shell contradicts the standard picture. If the charge was evenly distributed among all four Ce atoms, the valences would be $+2.79$ and $+3.26$ for the S_6 and i sites respectively.

The above picture from the BVM can be contrasted with the standard picture description of the same process, as illustrated in figures 13(c) and (d). Here, there are two ways one could assign the valences of the Ce sites in the divacancy. One way is to assign valences of $+4$ to three of the i sites, two on the first tetrahedron and one on the second. The remainder of the Ce sites are then assigned the valence of $+3$, as illustrated in figure 13(d)(i). An alternative arrangement of the charges is illustrated in figure 13(d)(ii). Here, the three $+4$ valences are assigned one each to one of the i sites from the first and second tetrahedra with the third being assigned to the S_6 site.

4.3. Comparison with calculations based on density functional theory

Most DFT calculations (performed in the supercell of composition $Ce_{32}O_{63}$) characterizing the location and character

Figure 13. Schematic illustrating the charge distribution following divacancy formation, based on a bond valence sum analysis of the crystal structures of CeO_2 and Ce_7O_{12}. (a) Part of the CeO_2 lattice showing two neighbouring O atoms (light grey (orange) circles), each inside a tetrahedron of Ce atoms (black circles). The numbers shown are the bond valence sums for each of the atoms. When the two neighbouring O atoms are removed due to the reduction of CeO_2, the divacancy of Ce_7O_{12} is formed as shown in (b). The bond valence sums on the Ce sites of triclinic symmetry (grey circles) have decreased from $+3.73$ in CeO_2 to $+3.21$ reflecting the presence of the additional charge left behind when the two O atoms are removed. The bond valence sum on the S_6 Ce site is virtually unchanged.

of the excess charge near bulk O vacancies concluded that the charge localizes on two of the nearest neighbour Ce ions [28, 17, 30, 48, 18, 49, 50, 12]. This is what we have called *the standard picture*. It appears that this picture was first brought into question by Castleton *et al* [32] in a paper where the question of charge localization was extensively explored. They concluded that it was not possible to fully localize the Ce 4f electrons on these Ce sites in the DFT + U framework while at the same time preserving a correct description for all the other electrons. We are not aware of any subsequent DFT+ U reports directly addressing this question in the conventional supercell. The more recent work used a periodic electrostatic embedded cluster method (PEECM) [51]. This work found that the charge preferred to localize well away from the O vacancy, being on Ce sites of the third coordination shell. As this shell coincided with the boundary of the quantum mechanical part of the cluster used in the calculation, the authors raised the possibility that the result may be an artefact of the method.

We also note that Burow *et al* [51] obtained three different Ce–Ce distances of 4.07, 4.12 and 4.20 Å in the first coordination shell. These distances are shorter than those reported in table 1 for the vacancy cluster of $Ce_{11}O_{20}$. However, since the structures in question are different, one should be cautious about such comparisons.

Our results are also in agreement with some recent reports on the location and localization of the excess electrons for surface and subsurface O vacancies [33, 34]. These authors argued that the localization of charge on next nearest neighbour Ce sites was mainly controlled by the lattice relaxation due to electrostatics, as reflected in the lowering of the Madelung potential. However, it should be remarked that a bulk O vacancy is in a different coordination environment relative to either a surface or subsurface O vacancy. It is therefore possible that the comparison between our results for bulk O vacancies and those reported for surface/subsurface O
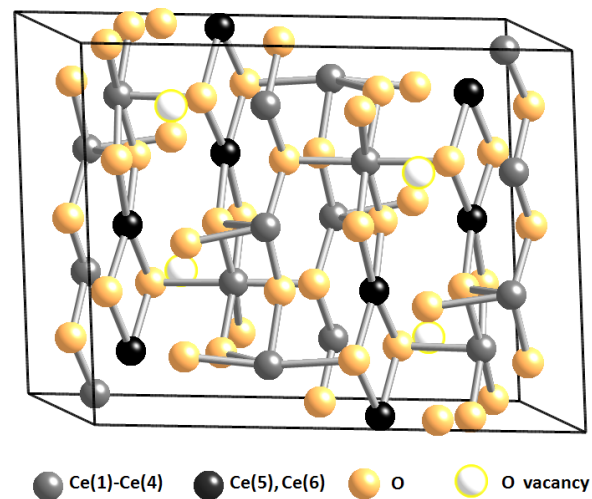
Figure 14. The unit cell of Ce_6O_{11} which consists of four formula units. The Bravais lattice is monoclinic and of space group $P2_1/c$.

vacancies may not be simple. Indeed, some authors have reported differences in the location of the charge between surface/subsurface and bulk O vacancies [51]. Nevertheless, it is interesting to note that, until these more recent results, the standard picture was considered applicable to surface and subsurface O vacancies as well [18, 49, 52].

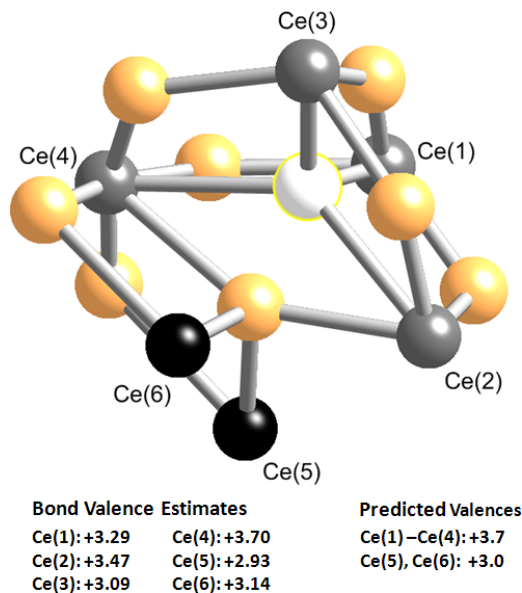## 5. Predicted charge distribution in Ce_6O_{11}

We make a few remarks about a possible charge distribution around the O vacancies in this crystal whose unit cell is shown in figure 14. Complete crystal structure data is not available but we make predictions of the charge distribution to be expected in this crystal from a generalization of the bond valence results

of Ce_7O_{12} and $Ce_{11}O_{20}$. The proposed vacancy cluster for studying the charge distribution in the local environment of the oxygen vacancy in this crystal is shown in figure 15. We did not find a full crystallographic characterization of this crystal and therefore it is not possible to perform accurate bond valence calculations for it. The results reported in **I** for this crystal were based on the positional parameters of Pr_6O_{11}. If one were to accept these results (table 1 of **I**), then since Ce(1), Ce(2), Ce(3) and Ce(4) coordinate the O vacancy with Ce(5) and Ce(6) in the second coordination shell for the Ce sublattice, we see that the charge distribution does not quite follow the pattern one would expect from the results obtained for $Ce_{11}O_{20}$ and Ce_7O_{12}. The overall charge in the vacancy cluster is larger by about ~ -1.2 compared to what one would expect starting from mixed valence CeO_2. This discrepancy is twice what we found in the case of $Ce_{11}O_{20}$ if the discrepancies are normalized to the total number of Ce sites in each vacancy cluster. As a result, the three Ce sites Ce(1), Ce(2) and Ce(3) which one would expect to have valences close to $+3.7$ have much lower valences. We do not believe that this is the correct charge distribution in the local environment of the O vacancy for this crystal. Instead, we prefer to extrapolate the argument which emerges from the bond valence results of $Ce_{11}O_{20}$ and Ce_7O_{12}. Doing so leads to the prediction that the correct charge distribution for this crystal should be as illustrated in figure 15, where all the charge goes to the two Ce sites in the second coordination shell i.e. Ce(5) and Ce(6). Of the known crystal structures of the reduced higher oxides of ceria, Ce_6O_{11} is the closest to the customary supercell used in DFT, in that it is the least reduced. The prediction we have made here would suggest that, except in an artificial way, it should not be possible to localize the electrons from the O vacancy site in the first coordination shell for the customary supercell used in DFT for studying this problem. An experiment giving the full crystallographic data for this phase would help resolve this question.

6. Delocalization via f–p hybridization

The possibility of the direct hopping of electrons between f-orbitals on neighbouring Ce sites has been suggested to explain the charge distribution in reduced ceria phases [43]. We briefly explore this suggestion considering the example of Ce_7O_{12}. There are two immediate questions one may like to answer about the charge distribution obtained for this phase from the bond valence calculations. First, how does an f-electron delocalize among the Ce(2) sites? Is this through direct f–f hopping or through the more indirect two-step process of f–p hopping which involves an O site bonded to both Ce sites? Second, why does this delocalization of the charge not extend to include the Ce(1) which is also in the same first coordination shell of the O vacancy? We are not in a position to give a detailed answer to these questions in the present paper, but only some preliminary indications based on Harrison's method of universal parameters [53]. We do not believe that the delocalization of the f level charge between the Ce(2) sites is a result of direct f–f coupling between these sites.

We now consider the two relevant cases, i.e., direct f–f hopping between neighbouring Ce sites and the indirect f–p hopping which involves an O site between the Ce sites in

Bond Valence Estimates   **Predicted Valences**

Ce(1): +3.29   Ce(4): +3.70   Ce(1)–Ce(4): +3.7
Ce(2): +3.47   Ce(5): +2.93   Ce(5), Ce(6): +3.0
Ce(3): +3.09   Ce(6): +3.14

Figure 15. The proposed vacancy cluster of Ce_6O_{11} consisting of the six Ce sites as shown. The sites Ce(1)–Ce(4) are in the first coordination shell of the O vacancy and are coordinated to seven O atoms. The Ce(5) and Ce(6) sites are in the second coordination shell and have the full eight-coordination of the Ce site in CeO_2. Bond valence sums are listed for each of these Ce sites as estimated from the positional parameters of Pr_6O_{11} and taken from **I**. We also show the site valences we predict from a generalization of the bond valence results of Ce_7O_{12} and $Ce_{11}O_{20}$.

question. In each of these cases, we consider two situations: electron hopping between two Ce(2) sites which delocalizes the charge between these sites and the electron hopping between a Ce(2) and a Ce(1) site which could also delocalize the charge between these sites.

For the case of direct f–f coupling, the relevant distances are: Ce(1)–Ce(2)—4.11 Å. These distances are quite comparable and they give the same direct f–f hopping matrix element, t_{ff}, estimated [53, 54] to be about 0.01 eV. This matrix element is the most favourable of all the four nonvanishing f–f matrix elements and represents a $\sigma-\sigma$ interaction between the two orbitals. This result would suggest that, if direct f–f coupling were the dominant mechanism of charge delocalization, then charge would delocalize over all four Ce atoms which are nearest neighbours to the O vacancy.

In the case of f–p hopping, we again, consider two cases: hopping along the Ce(1)–O(2)–Ce(2) bonds which we designate 'O(2) hopping' and the 'O(1) hopping' which occurs along Ce(2)–O(1)–Ce(2). For O(2) hopping, the respective matrix elements, t_{fp}, for electron hopping between Ce(1) and O(2) as well as O(2) and Ce(2) are [53, 55] 0.67 and 0.46 eV. These matrix elements refer to a $\sigma-\sigma$ interaction between the two orbitals which are the more favourable of the two nonvanishing matrix elements. Since, for f–p hopping to couple f states between two Ce sites, a two-step process involving the hopping of an f-electron from one Ce(2) site to an O 2p level followed by the hopping of an electron from the O 2p to the 4f level of the other Ce(2) site is required, the overall matrix element for O(2) hopping, t_{eff}, becomes 0.15 eV

calculated from equation (3).

$$t_{eff} = \frac{t_{fp}^2}{\varepsilon_f - \varepsilon_p} \qquad (3)$$

where we have assumed that the energy gap between the Ce 4f-
and the O 2p levels, $\varepsilon_f - \varepsilon_p$, is ∼2 eV [32]. The corresponding
matrix elements for O(1) hopping are 0.50, 0.61 and 0.15 eV
respectively. We see that the overall matrix element, t_{eff}, is
the same in the two cases. Again, this would suggest that the
charge should completely delocalize over all the Ce sites in the
divacancy, which contradicts the results of the bond valence
method. Thus, we conclude that the Harrison parameters
cannot fully explain the charge delocalization in the Ce_7O_{12}
divacancy. However, they appear to exclude the possibility of
direct f–f hopping, since t_{eff} is an order of magnitude larger
than t_{ff}. These approximate results give some indication of why
the charge delocalization may not extend to include the Ce(1)
site. An alternative way of looking at the indirect f–f coupling
is to view it as a hybridization of the 4f states at the two
Ce(2) sites and the O 2p states at the O atom connecting them
through Ce–O bonds. This indirect coupling is analogous to the
superexchange mechanism first discussed by McConnell [56].

7. Titanium and vanadium oxides

Ti oxides find uses in photocatalysis [57], gas sensing [58],
optical coatings [59], electrochemistry [60] and tribology [61].
The most important uses of V oxides are in industrial catalysis
with V_2O_5 as the main oxide phase [62].

Here, we treat the oxides of Ti and V together in order
to highlight some important similarities between some of
the oxides of these metals. In oxides, Ti and V exist in
formal oxidation states ranging from +2 to +4 and +2 to +5
respectively. This enables these metals to form several different
oxides with a rich variety of structural motifs. The more
important of these structures are classified into two distinct
homologous series of the type M_nO_{2n-1} and M_nO_{2n+1}, where
n is an integer and M = Ti or V. The first series constitutes
a class of oxides known as the Magnéli phases which have
also been identified in oxides of other metals, e.g., Mo, Nb
and W.

Our discussion here is limited only to the Magnéli phases,
where we explore the potential for the BVM to distinguish
between the insulating and metallic phases of these oxides.
Research in Magnéli phases of Ti and V is driven both by their
technological potential as well as the desire to understand the
fundamental science of the metal–insulator transition (MIT)
which occurs in these materials.

Technologically, Magnéli phases have been investigated
for their potential as host structures for superconductiv-
ity [63] and for their novel electrical and optical switching
properties. In VO_2, for example, a first-order structural
phase transition (SPT) occurs at 337 K which separates the
low temperature (LT) monoclinic phase (M_1) from the high
temperature (HT) tetragonal rutile phase (M_3) [64]. The
(M_1) phase is insulating while the (M_3) phase is metallic and,
therefore, the SPT of VO_2 is closely associated with the MIT

of this oxide, but as we discuss later, it is not well established
whether or not these two transitions coincide. The MIT is
accompanied by a change in the electrical conductivity of up
to five orders of magnitude [65–67] as well as a sharp change
in optical properties [68]. The (M_1) phase is transparent to
infrared radiation while the (M_3) phase is opaque [69]. The
novel electrical response across the MIT has been exploited in
critical thermistors and threshold switches [70]. The optical
switching for infrared light has found applications in switching
devices [69, 71] and smart thermochromic windows [72, 73].
Applications of V oxides have recently been reviewed by Wu
et al [74].

The fundamental understanding of the MIT in both the Ti
and V Magnéli phases is a complex many-body problem in
condensed matter physics and an active area of research. We do
not intend to review this area here (see, e.g., [75, 76]). Briefly,
explanations based on strong electronic correlations [77–80],
electron–phonon coupling [81–84] and a combination of both
effects [85–89] have been given.

In seeking to understand the crystal structures of the
Magnéli phases, one might hope to follow a similar approach
to that taken above for the Ce oxides; that is, one could
view them as resulting from the creation of O vacancies in
the dioxide structures, namely, TiO_2 and VO_2. However,
in contrast to the Ce oxides, where the Ce cation sublattice
remains largely invariant with reduction, there is significant
relaxation of the cation sublattices of the Magnéli phases
while the anion sublattices undergo only minimal change. As
a result, it has been proposed that for a unified treatment
of these crystal structures, a picture based on viewing these
structures as built around a rigid anion framework is more
informative [76]. In this framework, it is no longer possible
to discuss the O vacancies as point defects, as was done for the
Ce oxides. Instead, the defects are accommodated as ordered
long range structures called crystallographic shear (CS) planes
which separate slabs of composition MO_2. Each slab has
the rutile structure and is infinite in two dimensions with a
thickness of n O octahedra in the third. We will not discuss
any further the details of these structures, as these have been
extensively covered elsewhere (see e.g., [76]).

Since the analysis of the O defects in the crystal structures
of the Magnéli phases in terms of the CS planes does not
lend itself to an examination of the charge distribution near
O vacancies, we do not consider this problem here. We
restrict our discussion to the question of whether or not
the bond valence model could be used to predict the MIT
as a function of temperature (within a given phase) and
composition (across a homologous series). We note that BVM
results have already been reported for some of the phases
we discuss in this section but in all such cases the method
of Zachariasen was used [90]. The method of Zachariasen
is no longer widely used so we calculated all the results
reported in tables 2 and 3 self-consistently using the method
of Brown in a procedure described by Shoko *et al* [35]. We
also point out that there is some discussion in the literature of
the MIT of the Magnéli phases in terms of the BVM but what
we present here is a more comprehensive assessment of this
approach.

Table 2. Bond valence sums of the different Ti sites in the crystals of selected Magnéli phases, Ti_nO_{2n-1}, $n = 2$–4.

Site	Ti_2O_3 296 K	Ti_2O_3 713 K	Ti_3O_5 298 K	Ti_3O_5 514 K	Ti_4O_7 120 K	Ti_4O_7 140 K	Ti_4O_7 298 K
Ti1	3.0	3.0	3.0	3.4	3.1	3.4	3.5
Ti2	—	—	3.9	3.2	4.1	3.6	3.5
Ti3	—	—	3.3	—	3.1	3.5	3.6
Ti4	—	—	—	—	4.0	3.6	3.5
Reference	[91]	[91]	[97]	[96]	[93]	[93]	[93]

7.1. The Ti Magnéli phases

In this section, we discuss the three Ti Magnéli phases, which include Ti_2O_3, Ti_3O_5 and Ti_4O_7. Ti_2O_3 undergoes a continuous MIT around 400–600 K without a change in the crystal symmetry [91]. Ti_4O_7, which is one of the most widely studied Magnéli phases of Ti, undergoes two consecutive first-order electrical conductivity transitions. A LT semiconductor–semiconductor (SS) transition occurs at ~130 K which is followed by a HT semiconductor–metal transition at ~150 K [92–95]. Ti_3O_5 exhibits a MIT at 460 K which is accompanied by a SPT from the monoclinic LT- to the orthorhombic HT phase [96]. The BVS results calculated for the various Ti sites in these oxides are given in table 2.

In this table, the bottom row lists the references from which the crystallographic data was obtained. Both the LT and HT phases of Ti_2O_3 give a BVS of $+3.0$, which indicates that the changes in Ti–O bond lengths cannot explain the MIT in this oxide. One explanation that has been given for the MIT in Ti_2O_3 is that the shortening in some Ti–Ti distances leads to cation pairing [98, 85].

Table 2 shows that the respective Ti site valences in LT Ti_3O_5 are $+3.0$, $+3.9$ and $+3.3$, which should be compared to the corresponding formal valences of $+3.0$, $+4.0$ and $+3.0$ respectively. One then sees that the BVM results give a total Ti charge per formula unit (f.u.) of $+10.2$, whereas the formal result should be $+10.0$, giving an error of $+0.2$ charge/f.u. Nonetheless, with the exception of the Ti(3) site, the conclusion from the BVS is that the charges are localized. In the HT phase, only two distinct Ti sites exist and the BVS are $+3.4$ and $+3.2$ respectively. To understand how the charge redistributes itself in the HT- relative to the LT phase, one first notes that there are 4 f.u./unitcell in both the LT- and HT phases of Ti_3O_5. It is then evident that the Ti(1) and Ti(2) sites in the LT phase become the Ti(1) site in the HT phase. Thus, we immediately see that the electron which was localized on the Ti(1) site in the LT phase delocalizes between this and the Ti(2) site, which both become the Ti(1) site in the HT phase. Therefore, the overall conclusion from the BVM is that the MIT in Ti_3O_5 is a result of the change from localized to delocalized charge in the LT- and HT phases respectively.

The BVS for Ti_4O_7 show that the charge is localized in the low temperature (LT) phase whereas it is delocalized for both the intermediate temperature (IT) and high temperature (HT) phases. The results then suggest that the SS transition is explained by the change from localized to delocalized charge, whereas no explanation can be given for the MIT from these results. This scenario seems to be almost the opposite of what

one would expect. For a simple system, it is to be expected that the change to metallic conductivity would be associated with the transition from localized to delocalized charge. Thus, from this simple argument, one would expect both the IT- and HT phases to be metallic. However, Ti_4O_7 is not a simple system and the two phase transitions cannot be explained by the BVM. Considerable research effort has been directed at elucidating this problem and the picture that seems to emerge is that the changes which occur on the Ti sublattice may be more relevant for discussing the phase transitions [99, 84, 100, 101]. In the LT phase, Ti^{3+}–Ti^{3+} pairs form and these are covalently bonded. This results in a highly ordered structure of bipolarons on the Ti sublattice. The SS transition is then explained by the loss of the long range order of the bipolarons, giving a bipolaron liquid state in the IT phase. The transition from the IT semiconducting phase to the HT metallic phase is explained by charge delocalization. Since the BVM does not consider the bond length relationships within the Ti sublattice, it cannot capture the bipolaron formulation of the SS transition in Ti_4O_7. We remark here, however, that the picture we have just described for Ti_4O_7 was recently challenged [102]. In this report, it is argued that there is no bond formation between the Ti^{3+}–Ti^{3+} pairs in the LT and IT phases but that the main physics relates to a combination of strong electron correlations and electron–phonon coupling.
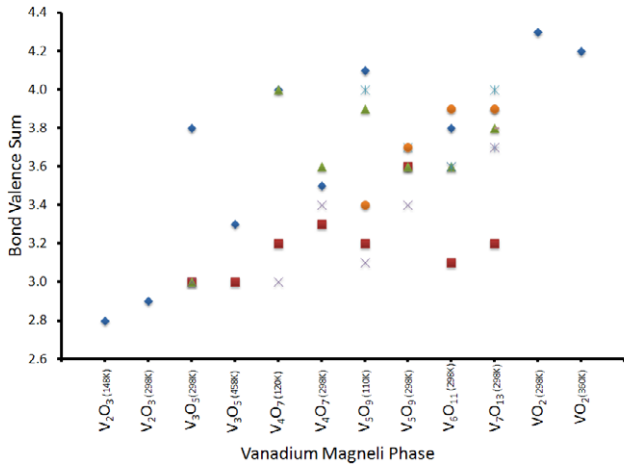
7.2. The V Magnéli Phases

Among the various Magnéli phases, the end members, V_2O_3 ($n = 1$) and VO_2 ($n = \infty$) along with V_4O_7 have been extensively studied in an effort to elucidate the microscopic mechanisms of the MIT which occur in these crystals. The MIT temperatures for the various Magnéli phases are as follows [76]: V_2O_3—168 K, V_3O_5—430 K, V_4O_7—250 K, V_5O_9—135 K, V_6O_{11}—170 K, V_7O_{13}—metallic and VO_2—340 K.

Our BVS results for the different V sites in selected crystals of the Magnéli phases of V are listed in table 3. For a discussion of the MIT, these results are presented as in figure 16, where the difference in the charge distribution between the insulating and metallic phases is clearer. The examples of V_4O_7 and V_5O_9 best illustrate the MIT within a given Magnéli phase as a function of temperature. In both cases, the insulating phases are characterized by a distinct bimodal charge distribution corresponding to localized valences of $+3$ and $+4$ respectively. In contrast, the corresponding metallic phases exhibit a delocalization of the charge, as can be seen from the clustering of the BVS near the value of the average stoichiometric valence.

V_3O_5 undergoes a MIT at 430 K which is accompanied by the $P2/c \rightarrow I2/c$ SPT [103, 104]. However, unlike in the other Magnéli phases, where the change in the electrical conductivity is several orders of magnitude, in this oxide, the change is only an order of magnitude [105]. The MIT is believed to be driven by charge differentiation and spatial ordering, with the LT phase charge-ordered while the HT phase exhibits charge disorder [103, 104]. For the LT phase, the BVM predicts that the charge localizes on the V sites giving the

Table 3. Bond valence sums of the different V sites in the crystals of selected Magnéli phases, V_nO_{2n-1}, $n = 3–7, \infty$.

Site	V_2O_3 148 K	V_2O_3 298 K	V_3O_5 298 K	V_3O_5 458 K	V_4O_7 120 K	V_4O_7 298 K	V_5O_9 110 K	V_5O_9 298 K	V_6O_{11} 298 K	V_7O_{13} 298 K	VO_2 298 K	VO_2 360 K
V1	2.8	2.9	3.8	3.3	4.0	3.5	4.1	3.6	3.8	3.9	4.3	4.2
V2	—	—	3.0	3.0	3.2	3.3	3.2	3.6	3.1	3.2	—	—
V3	—	—	3.0	—	4.0	3.6	3.9	3.6	3.6	3.8	—	—
V4	—	—	3.0	—	3.0	3.4	3.1	3.4	3.6	3.7	—	—
V5	—	—	—	—	—	—	4.0	3.7	3.6	4.0	—	—
V6	—	—	—	—	—	—	3.4	3.7	3.9	3.9	—	—
V7	—	—	—	—	—	—	—	—	—	3.7	—	—
V8	—	—	—	—	—	—	—	—	—	3.8	—	—
Reference	[107]	[108]	[103]	[104]	[109]	[110]	[111]	[111]	[112]	[112]	[113]	[114]

Figure 16. Bond valence sums for the different V sites in the crystal structures of the Magnéli phases. With the exception of V_2O_3 and VO_2, the results show that, within a given phase (see V_3O_5, V_4O_7 and V_5O_9), the charge delocalizes significantly in moving from the insulating to the metallic phase. For V_6O_{11} and V_7O_{13}, only results for the metallic phases are given. The results show that most of the charge is delocalized, which is consistent with the observed metallic conductivity.

following valences: V1—+3.8, V2–V4—+3.0 which agree well with the bond valence sums of Asbrink [103] obtained using the formula of Zachariasen [90]. In the HT, the LT V sites have collapsed as follows: V1, V2 → V1 and V3, V4 → V2. As pointed out by Hong and Asbrink [104], the ideal valence of V1 in the HT phase should be +3.5, or in our case, +3.4. Thus, the BVM suggests that the metallic conductivity observed in HT V_3O_5 results from the delocalization of the electron, which, in the LT phase, is localized at V2.

The results for the end members, V_2O_3 and VO_2, are not very informative, as the insulating phases are virtually indistinguishable from their metallic counterparts. It also appears that the BVM does not describe well the charge distribution in these oxides, giving values of +2.8 and +4.3 where +3.0 and +4.0 are the expected values respectively.

The results for V_6O_{11} and V_7O_{13} are given only for the room temperature phases. V_6O_{11} is known to undergo a MIT at 170 K, but we did not find crystallographic data for the insulating phase. Because V_7O_{13} is metallic at all temperatures, it is interesting for at least two reasons. First, if crystal structure data were available for low temperatures, say

<70 K, then obtaining BVS at the lower temperature would provide a good test for the BVM. If the charge were found to be delocalized at the lower temperature, then one would confidently conclude that the BVM is a good predictor of the MIT in these oxides. Secondly, since the higher Magnéli phases after V_7O_{13} undergo temperature-dependent MIT, e.g., V_8O_{15} (70 K) and VO_2 (340 K), this phase is unusual within the homologous series. Thus, the electronic conductivity of the Magnéli phases has a composition dependence which is such that there is a unique intermediate composition at which metallic conductivity occurs.

This composition dependence of the electronic conductivity in the Magnéli phases is remarkably similar to the prediction we made elsewhere about the Ce oxide phases of the Ce_nO_{2n-2} homologous series [106]. In that report, it was predicted that Ce_7O_{12} would exhibit metallic conductivity based on results of a bond valence analysis. If metallic conductivity is experimentally confirmed for Ce_7O_{12}, it is then quite curious that it occurs at the same value of n for the two completely different structures.

7.3. Comparison with calculations based on density functional theory

There are limited reports which discuss the question of what happens to the two electrons left in the crystal when a neutral O atom is removed from the crystal of the dioxide to form a given bulk Magnéli phase. Liborio and Harrison found that O point defects are only stable at very low concentrations [115]. Ganduglia-Pirovano *et al* [31] have reviewed DFT work on bulk O vacancies in reduced TiO_2 and VO_2 and the reader is referred to this review for details. It has to be noted that these calculations are not performed on supercells which do not correspond to any of the characterized crystal phases of the reduced dioxides. Thus one needs to be cautious about generalizing the supercell results to thermodynamic phases, e.g., those represented by the Magnéli phases. Nonetheless, we summarized the main results here.

For the reduced TiO_2, the picture from DFT-based calculations is unclear. Inconsistent conclusions have been reached by different groups. Results obtained include a localization of most of the excess charge on the O vacancy site [116], a localization on the nearest neighbour Ti sites [117], and a delocalization of the charge [118].

A study of bulk O vacancies in V_2O_{5-x} combining photoemission spectroscopy and DFT calculations concluded

that when a neutral O atom is removed from the perfect crystal, the two electrons that remain are shared between the vacancy site and the nearest V sites [119]. Of the total excess charge, 1.52 was found to remain on the vacancy site while 0.48 was shared among the nearest V sites.

7.4. Conclusion

The MIT and SS transitions in Magnéli phases of both Ti and V display some rich physics which may include strong electron correlations and strong electron–phonon coupling. Our BVM results suggest that for phases where strong electron correlations dominate the physics of the transition, the BVM could give a good prediction of the transition. On the other hand, for systems where the electron–phonon coupling on the cation sublattice controls the transition, the BVM gives no information about the physics. This is because the BVM does not take into account bond length relationships within the cation sublattice. Thus the BVM fails to describe phase transitions where bipolaron dynamics are important.

Finally, we remark that our results for the MIT of the oxides suggest that the MIT should coincide with the structural phase transition (SPT). However, the question of whether the MIT and the SPT coincide appears to still be an open problem and an active area of research. The case of VO_2 may be cited in this [120].

8. Conclusions and future directions

The main goal of this review was to answer the question: when an oxygen atom is removed from bulk cerium oxide where do the two excess electrons go? The approach taken was to consider high resolution crystal structures of $Ce_{11}O_{20}$ and Ce_7O_{12} and see how they could be viewed as ordered arrays of oxygen vacancies in an underlying CeO_2 crystal. The charge distribution in the local environments of the O vacancies can then be deduced from the bond valence model. An important conclusion is that the results are incompatible with the widely accepted standard picture of charge localization on two cerium ions next to the vacancy. Instead, we found that the charge distributes itself predominantly in the second coordination shell of cerium ions. Furthermore, one excess electron can be delocalized over more than one cerium ion.

Our conclusions concerning the charge distribution near oxygen vacancies are significant for several reasons. First, they contradict many (but not all) atomistic simulations based on density functional theory. Second, the actual charge distribution around the defect has important implications for the other questions we posed at the beginning of this review. The charge distribution has a significant effect on the relative stability of surface and subsurface vacancies [33]. Also, if the charge around oxygen surface and subsurface vacancies is not simply localized on Ce ions next to the vacancy this could change our understanding of the catalytic activity of these surfaces, since it has been claimed or assumed that it is associated with Ce^{3+} ions at the surface [121, 18]. The charge distribution around the vacancies has implications for electronic and ionic conduction, a subject we have discussed elsewhere [106].

Since our determination of the charge distribution around vacancies is indirect it will be important to see whether the same conclusions are obtained on experiments on these higher order oxides with complementary probes such as magnetic susceptibility [122], electron spin resonance (ESR), nuclear magnetic resonance, and photoemission spectroscopies. For example, ESR spectra [123] should quite be distinct for the standard picture of electrons localized onto Ce^{3+} ions and our alternative picture of partial delocalization over the second coordination shell and unique charge (and spin) distributions associated with single vacancies and divacancies.

A variety of spectroscopic probes have shown that the formation of oxygen vacancies is also associated with new electronic states which are located in energy between the valence band of nominally 'oxygen 2p' states and the 'localized 4f' states. [124, 125] DFT-based calculations which do not sufficiently include the effect of electronic correlations fail to produce these states [31]. Generally the energy of defect states is correlated with the extent of electron localization around defects. Hence, we suggest that spectroscopic studies of ordered phases of higher order oxides could be a fruitful approach to characterizing the electronic properties of defects and complementary to the structural approach we have reviewed. We expect that the energies of the electronic states associated with each of the vacancies we have considered will be different and correlated with the extent of charge delocalization that we find. Such experimental results will provide significant constraints on theories.

Another objective of this review was to test the bond valence analysis on transition metal oxides. For this, we selected the Magnéli phases of Ti and V which are crystallographically well-characterized from their single crystals. Discussing the charge distribution near O vacancies in these oxides (as was done for the Ce oxides) was not possible because the O vacancies in these oxides do not occur as point defects. Rather, they are accommodated into the structure as crystallographic shear planes which do not lend themselves to such an analysis. We, however, addressed the important question of the change in the charge distribution across a MIT in these oxides. The main result from this was that, for crystal structures where the M–O bond lengths undergo significant changes in moving from the insulating to the metallic phase, the BVM provides a useful guide for understanding some of the microscopic physics involved.

This review only considered bulk cerium, titanium and vanadium oxides. However, we believe our approach to characterizing electronic properties of oxygen vacancies in terms of a bond valence sum analysis and the physical insights gained should also be fruitful in the study of surface defects and to other widely studied oxides such as those of hafnium and zirconium.

A common theme throughout this review is the question of whether or not the valence d and f electrons localize on metal sites or delocalize throughout the crystal. This may bring to mind the well-known question of whether a valence bond or molecular orbital (MO) picture is the more appropriate description for the electronic properties of molecules. For an interesting and entertaining conversation on this debate,

see [46]. How is this broader question, relevant? First, VB theory tends to localize electrons too much. Molecular orbital MO theory tends delocalize electrons too much. Second, our empirical valence bond sum approach is a very local picture and somehow capturing the same physics and chemistry as VB theory. Third, LDA is close to MO theory (it is a band theory, i.e., a non-local picture) and tends to delocalize electrons too much. Many of the LDA, and LDA $+ U$ calculations on cerium oxides artificially force electrons to localize on cerium ions. Finally, it is interesting that such VB versus MO issues were discussed in Mott's original paper on the metal–insulator transition [126].

Acknowledgments

References

[1] Singhal S C and Kendall K (ed) 2003 *High Temperature Solid Oxide Fuel Cells: Fundamentals, Design and Applications* (Amsterdam: Elsevier)

[2] Inaba H and Tagawa H 1996 Ceria-based solid electrolytes *Solid State Ion.* **83** 1–16

[3] Steele B C H 2000 Appraisal of $Ce_{1-y}Gd_yO_{2-y/2}$ electrolytes for IT-SOFC operation at 500 °C *Solid State Ion.* **129** 95–110

[4] Kharton V V, Figueiredo F M, Navarro L, Naumovich E N, Kovalevsky A V, Yaremchenko A A, Viskup A P, Carneiro A, Marques F M B and Frade J R 2001 Ceria-based materials for solid oxide fuel cells *J. Mater. Sci.* **36** 1105–17

[5] Zhang D-E, Zhang X-J, Ni X-M, Song J-M and Zheng H-G 2006 Optical and electrochemical properties of CeO_2 spindles *ChemPhysChem* **7** 2468–70

[6] Trovarelli A (ed) 2002 *Catalysis by Ceria and Related Materials* (Singapore: World Scientific)

[7] Blank J H, Beckers J, Collignon P F and Rothenberg G 2007 Redox kinetics of ceria-based mixed oxides in selective hydrogen combustion *ChemPhysChem* **8** 2490–7

[8] Chen H-T, Choi Y M, Liu M and Lin M C 2007 A theoretical study of surface reduction mechanisms of $CeO_2(111)$ and (110) by H_2 *ChemPhysChem* **8** 849–55

[9] Mo L, Zheng X and Yeh C-T 2005 A novel CeO_2/ZnO catalyst for hydrogen production from the partial oxidation of methanol *ChemPhysChem* **6** 1470–2

[10] Fray D J 2001 Solid-state gas sensors *Encyclopedia of Materials: Science and Technology* ed K H J Buschow, R W Cahn, M C Flemings, B Ilschner, E J Kramer and S Mahajan (Oxford: Elsevier) pp 8726–30

[11] Jasinski P, Suzuki T and Anderson H U 2003 Nanocrystalline undoped ceria oxygen sensor *Sensors Actuators* B **95** 73–7

[12] Keating P R L, Scanlon D O and Watson G W 2009 Intrinsic ferromagnetism in CeO_2: dispelling the myth of vacancy site localization mediated superexchange *J. Phys.: Condens. Matter* **21** 405502

[13] Song Y Q, Zhang H W, Yang Q H, Liu Y L, Li Y X, Shah L R, Zhu H and Xiao J Q 2009 Electronic structure and magnetic properties of Co-doped CeO_2: based on first principle calculation *J. Phys.: Condens. Matter* **21** 125504

[14] Farhan M A and Akhtar M J 2010 Negative pressure driven phase transformation in Sr doped $SmCoO_3$ *J. Phys.: Condens. Matter* **22** 075402

[15] Majumdar S, Ray P, Ganguly S and Kargupta K 2009 On electroneutrality condition inside solid conducting porous film *AIChE* **55** 3026

[16] Hoskins B F and Martin R L 1995 The structure of higher rare earth oxides: role of the coordination defect *Aust. J. Chem.* **48** 709–39

[17] Skorodumova N V, Simak S I, Lundqvist B I, Abrikosov I A and Johansson B 2002 Quantum origin of the oxygen storage capability of ceria *Phys. Rev. Lett.* **89** 166601

[18] Esch F, Fabris S, Zhou L, Montini T, Africh C, Fornasiero P, Comelli G and Rosei R 2005 Electron localization determines defect formation on ceria substrates *Science* **309** 752–5

[19] Kroger F A and Vink H J 1956 Relations between the concentrations of imperfections in crystalline solids *Solid State Phys.* **3** 307

[20] Martin R L 1974 Structural theory for non-stoichiometry. Part 1. Defect fluorite-type structures: lanthanoid oxides MO_x with $1.7 \leqslant x \leqslant 2.0$ *J. Chem. Soc., Dalton Trans.* 1335

[21] Kang Z C, Zhang J and Eyring L 1996 The structural principles that underlie the higher oxides of the rare earths *Z. Anorg. Allg. Chem.* **622** 465–72

[22] Thornton G and Dempsey M J 1981 Final-state effects in the 3d and 4d x-ray photoelectron spectra of CeO_2 *Chem. Phys. Lett.* **77** 409

[23] Fujimori A 1983 Mixed-valent ground state of CeO_2 *Phys. Rev.* B **28** 2281

[24] Kotani A, Mizuta H, Jo T and Parlebas J C 1985 Theory of core photoemission spectra in CeO_2 *Solid State Commun.* **53** 805–10

[25] Kotani A, Jo T and Parlebas J C 1988 Many-body effects in core-level spectroscopy of rare-earth compounds *Adv. Phys.* **37** 37–85

[26] Kotani A 2005 Resonant inelastic x-ray scattering in d and f electron systems *Eur. Phys. J.* B **47** 3–27

[27] Sham T K, Gordon R A and Heald S M 2005 Resonant inelastic x-ray scattering at the Ce L_3 edge of $CePO_4$ and CeO_2: implications for the valence of CeO_2 and related phenomena *Phys. Rev.* B **72** 035113

[28] Skorodumova N V, Ahuja R, Simak S I, Abrikosov I A, Johansson B and Lundqvist B I 2001 Electronic, bonding and optical properties of CeO_2 and Ce_2O_3 from first principles *Phys. Rev.* B **64** 115108

[29] Mogensen M, Sammes N M and Tompsett G A 2000 Physical, chemical and electrochemical properties of pure and doped ceria *Solid State Ion.* **129** 63–94

[30] Fabris S, de Gironcoli S, Baroni S, Vicario G and Balducci G 2005 Taming multiple valency with density functionals: a case study of defective ceria *Phys. Rev.* B **71** 041102

[31] Ganduglia-Pirovano M V, Hofmann A and Sauer J 2007 Oxygen vacancies in transition metal and rare earth oxides: current state of understanding and remaining challenges *Surf. Sci. Rep.* **62** 219–70

[32] Castleton C W M, Kullgren J and Hermansson K 2007 Tuning LDA $+ U$ for electron localization and structure at oxygen vacancies in ceria *J. Chem. Phys.* **127** 244704

[33] Ganduglia-Pirovano M V, Da Silva J L F and Sauer J 2009 Density-functional calculations of the structure of near-surface oxygen vacancies and electron localization on $CeO_2(111)$ *Phys. Rev. Lett.* **102** 026101

16

[34] Li H-Y, Wang H-F, Gong X-Q, Guo Y-L, Guo Y, Lu G and Hu P 2009 Multiple configurations of the two excess 4f electrons on defective $CeO_2(111)$: origin and implications *Phys. Rev.* B **79** 193401

[35] Shoko E, Smith M F and McKenzie R H 2009 Mixed valency in cerium oxide crystallographic phases: valence of different cerium sites by the bond valence method *Phys. Rev.* B **79** 134108

[36] Kang Z C and Eyring L 1997 The structural basis of the fluorite-related rare earth higher oxides *Aust. J. Chem.* **49** 981–96

[37] Zinkevich M, Djurovic D and Aldinger F 2006 Thermodynamic modelling of the cerium–oxygen system *Solid State Ion.* **177** 989–1001

[38] Kang Z C and Eyring L 1998 The prediction of the structure of members of the homologous series of the higher rare earth oxides *J. Alloys Compounds* **275–277** 30–6

[39] Lopez-Cartes C, Perez-Omil J A, Pintado J M, Calvino J J, Kang Z C and Eyring L 1999 Rare-earth oxides with fluorite-related structures: their systematic investigation using HREM images, image simulations and electron diffraction pattern simulations *Ultramicroscopy* **80** 19–39

[40] Bevan D J M and Martin R L 2008 The role of the coordination defect: a new structural description of four fluorite-related sesquioxide minerals, bixbyte (Mn_2O_3), braunite (Mn_7SiO_{12}), braunite ii ($CaMn_{14}O_{24}$), parwelite ($Mn_{10}Sb_2As_2Si_2O_{24}$), and their structural relationships *J. Solid State Chem.* **181** 2250–9

[41] Martin R L 1997 Defect fluorite-type structures: modelling lanthanoid oxides *Chem. Soc., Dalton Trans.* 3659–70

[42] Kummerle E A and Heger G 1999 The structures of $C-Ce_2O_{3+\delta}$, Ce_7O_{12}, and $Ce_{11}O_{20}$ *J. Solid State Chem.* **147** 485

[43] Zhang J, Von Dreele R B and Eyring L 1993 The structure of Tb_7O_{12} and $Tb_{11}O_{20}$ *J. Solid State Chem.* **104** 21–32

[44] Ray S P and Cox D E 1975 Neutron diffraction determination of the crystal structure of Ce_7O_{12} *J. Solid State Chem.* **15** 333

[45] Shannon R D 1976 Revised effective ionic radii and systematic studies of interatomic distances in halides and chalcogenides *Acta Crystallogr.* A **32** 751

[46] Hoffmann R, Shaik S and Hiberty P C 2003 A conversation on VB vs MO theory: a never-ending rivalry? *Acc. Chem. Res.* **36** 750–6

[47] Liebau F, Wang X and Liebau W 2009 Stoichiometric valence and structural valence—two different sides of the same coin: 'bonding power' *Chemistry* **15** 2728–37

[48] Kresse G, Blaha P, Da Silva J L F and Ganduglia-Pirovano M V 2005 Comment on 'taming multiple valency with density functionals: a case study of defective ceria' *Phys. Rev.* B **72** 237101

[49] Nolan M, Fearon J E and Watson G W 2006 Oxygen vacancy formation and migration in ceria *Solid State Ion.* **177** 3069–74

[50] Andersson D A, Simak S I, Johansson B, Abrikosov I A and Skorodumova N V 2007 Modelling of CeO_2, Ce_2O_3, and CeO_{2-x} in the $LDA + U$ formalism *Phys. Rev.* B **75** 035109

[51] Burow A M, Sierka M, Döbler J and Sauer J 2009 Point defects in CaF_2 and CeO_2 investigated by the periodic electrostatic embedded cluster method *J. Chem. Phys.* **130** 174710

[52] Torbrugge S, Reichling M, Ishiyama A, Morita S and Custance O 2007 Evidence of subsurface oxygen vacancy ordering on reduced $CeO_2(111)$ *Phys. Rev. Lett.* **99** 056101

[53] Harrison W A 2004 *Elementary Electronic Structure* (Singapore: World Scientific)

[54] Harrison WalterA 1983 Electronic structure of f-shell metals *Phys. Rev.* B **28** 550–9

[55] Harrison W A and Straub G K 1987 Electronic structure and properties of d- and f-shell-metal compounds *Phys. Rev.* B **36** 2695–706

[56] McConnell H M 1961 Intramolecular charge transfer in aromatic free radicals *J. Chem. Phys.* **35** 508–15

[57] Fujishima A and Honda K 1972 Electrochemical photolysis of water at a semiconductor electrode *Nature* **238** 37–8

[58] Komem Y, Ankonina G, Rothschild A, Im J S and Chung U-J 2007 Titanium oxide thin film gas sensors *Phys. Scr.* **T129** 157–9

[59] Diebold U 2003 The surface science of titanium dioxide *Surf. Sci. Rep.* **48** 53–229

[60] Smith J R, Walsh F C and Clarke R L 1998 Electrodes based on Magnéli phase titanium oxides: the properties and applications of Ebonex materials *J. Appl. Electrochem.* **28** 1021–33

[61] Storz O, Gasthuber H and Woydt M 2001 Tribological properties of thermal-sprayed Magnéli-type coatings with different stoichiometries (Ti_nO_{2n-1}) *Surf. Coat. Technol.* **140** 76–81

[62] Weckhuysen B M and Keller D E 2003 Chemistry, spectroscopy and the role of supported vanadium oxides in heterogeneous catalysis *Catal. Today* **78** 25–46

[63] Marezio M, Gauzzi A, Licci F and Gilioli E 2000 Can the structure of the Ti or V Magnéli binary oxides host superconductivity? *Physica* C **338** 1–8

[64] Morin F J 1959 Oxides which show a metal–insulator transition at the Neel temperature *Phys. Rev. Lett.* **3** 34–6

[65] Santulli A C, Xu W, Parise J B, Wu L, Aronson M C, Zhang F, Nam C, Black C T, Tianoa A L and Wong S S 2009 Synthesis and characterization of V_2O_3 nanorods *Phys. Chem. Chem. Phys.* **11** 3718–26

[66] Qazilbash M M, Schafgans A A, Burch K S, Yun S J, Chae B G, Kim B J, Kim H T and Basov D N 2008 Electrodynamics of the vanadium oxides VO_2 and V_2O_3 *Phys. Rev.* B **77** 115121

[67] Corr S A, Grossman M, Furman J D, Melot B C, Cheetham A K, Heier K R and Seshadri R 2008 Controlled reduction of vanadium oxide nanoscrolls: crystal structure, morphology, and electrical properties *Chem. Mater.* **20** 6396–404

[68] Ruzmetov D, Zawilski K T, Senanayake S D, Narayanamurti V and Ramanathan S 2008 Infrared reflectance and photoemission spectroscopy studies across the phase transition boundary in thin film vanadium dioxide *J. Phys.: Condens. Matter* **20** 465204

[69] Baum P, Yang D and Zewail A H 2007 4D visualization of transitional structures in phase transformations by electron diffraction *Science* **318** 788

[70] Ivon A I, Kolbunov V R and Chernenko I M 1999 Stability of electrical properties of vanadium dioxide based ceramics *J. Eur. Ceramic Soc.* **19** 1883–8

[71] Cui J, Da D and Jiang W 1998 Structure characterization of vanadium oxide thin films prepared by magnetron sputtering methods *Appl. Surf. Sci.* **133** 225

[72] Duchene J 1975 Direct infrared measurements of filament transient temperature during switching in vanadium oxide film devices *J. Solid State Chem.* **12** 303–6

[73] Jin P, Nakao S and Tanemura S 1998 Tungsten doping into vanadium dioxide thermochromic films by high-energy ion implantation and thermal annealing *Thin Solid Films* **324** 151–8

[74] Wu C, Wei H, Ning B and Xie Y 2010 New vanadium oxide nanostructures: controlled synthesis and their smart electrical switching properties *Adv. Mater.* **22** 1–5

[75] Imada M, Fujimori A and Tokura Y 1998 Metal–insulator transitions *Rev. Mod. Phys.* **70** 1039–63

[76] Schwingenschlogl U and Eyert V 2004 The vanadium Magnéli phases V_nO_{2n-1} *Ann. Phys.* **13** 475–510

[77] Limelette P, Georges A, Jérome D, Wzietek P, Metcalf P and Honig J M 2003 Universality and critical behavior at the Mott transition *Science* **302** 89–92

[78] Tomczak J M and Biermann S 2009 Optical properties of correlated materials or why intelligent windows may look dirty *Phys. Status Solidi* B **246** 1996–2005

[79] Zylbersztejn A and Mott N F 1975 Metal–insulator transition in vanadium dioxide *Phys. Rev.* B **11** 4383–95

[80] Gatti M, Bruneval F, Olevano V and Reining L 2007 Understanding correlations in vanadium dioxide from first principles *Phys. Rev. Lett.* **99** 266402

[81] Goodenough J B 1971 *J. Solid State Chem.* **3** 490

[82] Vikhnin V S, Lysenko S, Rua A, Fernandez F and Liu H 2005 The model of metal–insulator phase transition in vanadium oxide *Phys. Lett.* A **343** 446–53

[83] Baldassarre L, Perucchi A, Arcangeletti E, Nicoletti D, Di Castro D, Postorino P, Sidorov V A and Lupi S 2007 Electrodynamics near the metal-to-insulator transition in V_3O_5 *Phys. Rev.* B **75** 245108

[84] Watanabe M, Ueno W and Hayashi T 2007 Optical study of metal–insulator transitions in Ti_4O_7 single crystals *J. Lumin.* **122/123** 393–5

[85] Tanaka A 2004 On the metal–insulator transitions in VO_2 and Ti_2O_3 from a unified viewpoint *J. Phys. Soc. Japan* **73** 152–62

[86] Tanaka A 2004 Theory on metal–insulator transitions and inverse photoemission spectroscopy in VO_2 and Ti_2O_3 *Physica* B **351** 240–4

[87] Vikhnin V S, Lysenko S, Rua A, Fernandez F and Liu H 2007 Charge transfer model of metal–insulator phase transition and ultrafast optical response in VO_2 *Opt. Mater.* **29** 1385–9

[88] Tomczak J M, Aryasetiawan F and Biermann S 2008 Effective bandstructure in the insulating phase versus strong dynamical correlations in metallic VO_2 *Phys. Rev.* B **78** 115103

[89] Tomczak J M and Biermann S 2009 Optical properties of correlated materials: generalized Peierls approach and its application to VO_2 *Phys. Rev.* B **80** 085117

[90] Zachariasen W H 1954 Crystal chemical studies of the 5f-series of elements. XXIII. On the crystal chemistry of uranyl compounds and related compounds of transuranic elements *Acta Crystallogr.* **7** 795–9

[91] Rice C E and Robinson W R 1976 Structural changes associated with the semiconductor-to-metal transition in Ti_2O_3 *Mater. Res. Bull.* **11** 1355–60

[92] Bartholomew R F and Frankl D R 1969 Electrical properties of some titanium oxides *Phys. Rev.* **187** 828–33

[93] Marezio M, McWhan D B, Dernier P D and Remeika J P 1973 Structural aspects of the metal–insulator transitions in T_4O_7 *J. Solid State Chem.* **6** 213–21

[94] Lakkis S, Schlenker C, Chakraverty B K, Buder R and Marezio M 1976 Metal–insulator transitions in Ti_4O_7 single crystals: crystal characterization, specific heat and electron paramagnetic resonance *Phys. Rev.* B **14** 1429

[95] Le Page Y and Marezio M 1984 Structural chemistry of Magnéli phases Ti_nO_{2n-1} $(4 \leqslant n \leqslant 9)$. IV superstructure in Ti_4O_7 at 140 K *J. Solid State Chem.* **53** 13–21

[96] Onoda M 1998 Phase transitions of Ti_3O_5 *J. Solid State Chem.* **136** 67–73

[97] Asbrink S and Magnéli A 1959 Crystal structure studies on trititanium pentoxide, Ti_3O_5 *Acta Crystallogr.* **12** 575–81

[98] Rice C E and Robinson W R 1977 *Acta Crystallogr.* B **33** 1342

[99] Eyert V, Schwingenschlögl U and Eckern U 2004 Charge order, orbital order, and electron localization in the Magnéli phase Ti_4O_7 *Chem. Phys. Lett.* **390** 151–6

[100] Watanabe M and Ueno W 2006 Raman study of order-disorder transition of bipolarons in Ti_4O_7 *Phys. Status Solidi* c **3** 3456–9

[101] Leonov I, Yaresko A N, Antonov V N, Schwingenschlögl U and Eyert V 2006 Charge order and spin-singlet pair formation in Ti_4O_7 *J. Phys.: Condens. Matter* **18** 10955–64

[102] Liborio L and Harrison N 2009 Electronic structure of the Ti_4O_7 Magnéli phase *Phys. Rev.* B **79** 245133

[103] Asbrink S 1980 The crystal structure and valency distribution in the low-temperature modification of V_3O_5. The decisive importance of a few very weak reflections in a crystal-structure determination *Acta Crystallogr.* B **36** 1332–9

[104] Hong S-H and Asbrink S 1982 The structure of the high temperature modification of V_3O_5 at 458 K *Acta Crystallogr.* B **38** 713

[105] Terukov E I, Chudnovskii F A, Reichelt W, Oppermann H, Bruückner W, Bruückner H P and Moldenhauer W 1976 Investigation of the physical properties of V_3O_5 at phase transition with consideration of its range of homogeniety *Phys. Status Solidi* a **37** 541–6

[106] Shoko E, Smith M F and McKenzie R H 2009 A consistent picture of the charge distribution in reduced ceria phases arXiv:0910.0669v2 [cond-mat.str-el]

[107] Dernier P D and Marezio M 1970 Crystal structure of the low-temperature antiferromagnetic phase of V_2O_3 *Phys. Rev.* B **2** 3771–6

[108] Dernier P D 1970 The crystal structure of V_2O_3 and $(V_{0.962}Cr_{0.038})_2O_3$ near the metal–insulator transition *J. Phys. Chem. Solids* **31** 2569–75

[109] Hodeau J and Marezio M 1978 The crystal structure of V_4O_7 at 120 °K *J. Solid State Chem.* **23** 253–63

[110] Marezio M, McWhan D B, Dernier P D and Remeika J P 1973 Structural aspects of the metal–insulator transition in V_4O_7 *J. Solid State Chem.* **6** 419–29

[111] Marezio M, Dernier P D, McWhan D B and Kachi S 1974 Structural aspects of the metal–insulator transition in V_5O_9 *J. Solid State Chem.* **11** 301–13

[112] Horiuchi H, Morimoto N and Tokonami M 1976 Crystal structures of V_nO_{2n-1} $(2 \leqslant n \leqslant 7)$ *J. Solid State Chem.* **17** 407–24

[113] Longo J M and Kierkegaard P 1970 A refinement of the structure of VO_2 *Acta Chem. Scand.* **24** 420–6

[114] McWhan D B, Marezio M, Remeika J P and Dernier P D 1974 X-ray diffraction study of metallic VO_2 *Phys. Rev.* B **10** 490–5

[115] Liborio L and Harrison N 2008 Thermodynamics of oxygen defective Magnéli phases in rutile: a first-principles study *Phys. Rev.* B **77** 104104

[116] Mackrodt W C, Simson E A and Harrison N M 1997 An *ab initio* Hartree–Fock study of the electron-excess gap states in oxygen-deficient rutile TiO_2 *Surf. Sci.* **384** 192

[117] Lindan P J D, Harrison N M, Gillan M J and White J A 1997 First-principles spin-polarized calculations on the reduced and reconstructed $TiO_2(110)$ surface *Phys. Rev.* B **55** 15919

[118] Cho E, Han S, Ahn H-S, Lee K-R, Kim S K and Hwang C S 2006 First principle study of defects in rutile TiO_{2-x} *Phys. Rev.* B **73** 193202

[119] Li Z-Y and Wu Q-H 2009 The effects of oxygen vacancies on the electronic properties of V_2O_{5-x} *J. Mater. Sci: Mater. Electron.* **19** S366–70

[120] Kim H-T, Lee Y W, Kim B-J, Chae B-G, Yun S J, Kang K-Y, Han K-J, Yee K-J and Lim Y-S 2006 Monoclinic and correlated metal phase in VO_2 as evidence of the Mott transition: coherent phonon analysis *Phys. Rev. Lett.* **97** 266401

[121] Campbell C T and Peden C H F 2005 Oxygen vacancies and catalysis on ceria surfaces *Science* **309** 713

[122] Perrichon V, Laachir A, Bergeret G, Frety R, Tournayan L and Touret O 1994 Reduction of cerias with different textures by hydrogen and their reoxidation with oxygen *J. Chem. Soc., Faraday Trans.* **90** 773

[123] Dutta P, Pal S, Seehra M S, Shi Y, Eyring E M and Ernst R D 2006 Concentration of Ce^{3+} and oxygen vacancies in cerium oxide nanoparticles *Chem. Mater.* **18** 5144–6

[124] Mullins D R, Radulovic P V and Overbury S H 1998 Electron spectroscopy of single crystal and polycrystalline cerium oxide surfaces *Surf. Sci.* **409** 307

[125] Henderson M A, Perkins C L, Engelhard M H, Thevuthasan S and Peden C H F 2003 Redox properties of water on the oxidized and reduced surfaces of $CeO_2(111)$ *Surf. Sci.* **526** 1–18

[126] Mott N F 1949 The basis of the electron theory of metals, with special reference to the transition metals *Proc. Phys. Soc.* A **62** 416–22